# Assessing the impacts of assimilating IASI and MOPITT CO retrievals using CESM-CAM-chem and DART

Jérôme Barré, Benjamin Gaubert, Avelino F. J. Arellano, Helen M. Worden, David P. Edwards, Merritt N. Deeter, Jeffrey L. Anderson, Kevin Raeder, Nancy Collins, Simone Tilmes, et al.

AGU PUBLICATIONS

JGR

Journal of Geophysical Research: Atmospheres

RESEARCH ARTICLE
10.1002/2015JD023467

**Key Points:**
- Chemical data assimilation in a global climate model
- Assimilation of nadir retrieved CO profiles
- Assessment of MOPITT and IASI CO capabilities for chemical weather

**Supporting Information:**
- Figures S1–S4

**Correspondence to:**
J. Barré,
barre@ucar.edu

**Citation:**
Barré, J., et al. (2015), Assessing the impacts of assimilating IASI and MOPITT CO retrievals using CESM-CAM-chem and DART, *J. Geophys. Res. Atmos.*, *120*, 10,501–10,529, doi:10.1002/2015JD023467.

Received 2 APR 2015
Accepted 17 AUG 2015
Accepted article online 21 AUG 2015
Published online 5 OCT 2015



# Assessing the impacts of assimilating IASI and MOPITT CO retrievals using CESM-CAM-chem and DART

**Jérôme Barré[1], Benjamin Gaubert[1], Avelino F. J. Arellano[2], Helen M. Worden[1], David P. Edwards[1], Merritt N. Deeter[1], Jeffrey L. Anderson[3], Kevin Raeder[3], Nancy Collins[3], Simone Tilmes[1], Gene Francis[1], Cathy Clerbaux[4,5], Louisa K. Emmons[1], Gabriele G. Pfister[1], Pierre-François Coheur[5], and Daniel Hurtmans[5]**

[1]Atmospheric Chemistry Observations and Modeling Laboratory, National Center for Atmospheric Research, Boulder, Colorado, USA, [2]Department of Atmospheric Science, University of Arizona, Tucson, Arizona, USA, [3]Institute for Mathematics Applied to Geoscience, National Center for Atmospheric Research, Boulder, Colorado, USA, [4]UPMC Université Paris 6, Université Versailles St-Quentin, LATMOS-IPSL, CNRS/INSU, Paris, France, [5]Spectroscopie de l'Atmosphère, Service de Chimie Quantique et Photophysique, Université Libre de Bruxelles, Brussels, Belgium

**Abstract** We show the results and evaluation with independent measurements from assimilating both MOPITT (Measurements Of Pollution In The Troposphere) and IASI (Infrared Atmospheric Sounding Interferometer) retrieved profiles into the Community Earth System Model (CESM). We used the Data Assimilation Research Testbed ensemble Kalman filter technique, with the full atmospheric chemistry CESM component Community Atmospheric Model with Chemistry. We first discuss the methodology and evaluation of the current data assimilation system with coupled meteorology and chemistry data assimilation. The different capabilities of MOPITT and IASI retrievals are highlighted, with particular attention to instrument vertical sensitivity and coverage and how these impact the analyses. MOPITT and IASI CO retrievals mostly constrain the CO fields close to the main anthropogenic, biogenic, and biomass burning CO sources. In the case of IASI CO assimilation, we also observe constraints on CO far from the sources. During the simulation time period (June and July 2008), CO assimilation of both instruments strongly improves the atmospheric CO state as compared to independent observations, with the higher spatial coverage of IASI providing better results on the global scale. However, the enhanced sensitivity of multispectral MOPITT observations to near surface CO over the main source regions provides synergistic effects at regional scales.

## 1. Introduction

Carbon monoxide (CO) is a primary criteria pollutant, with both natural and anthropogenic sources, and plays an important role in tropospheric chemistry and climate [*Kanakidou and Crutzen*, 1999; *Myhre et al.*, 2013, Intergovernmental Panel on Climate Change Fifth Assessment Report]. It is directly emitted as a product of incomplete combustion from industrial and urban fossil/biofuel burning as well as large-scale biomass burning and to a lesser extent directly emitted by plants and oceans. CO is also produced in the atmosphere by photochemical oxidation of anthropogenic and biogenic volatile organic compounds (VOC). This constitutes a large secondary source of CO especially in the tropics [*Griffin et al.*, 2007]. The reaction of CO with the hydroxyl radical (OH), which is the main oxidant in the troposphere, is considered the principal sink of CO. OH is also strongly tied with the production of CO through its oxidation of $CH_4$ and other hydrocarbons. Hence, the abundance of CO (and its associated lifetime in the troposphere) is inversely proportional to OH distribution [*Shindell et al.*, 2006]. For example, the longer lifetime (less OH) and larger emissions during winter are responsible for observed peaks in CO during March in the Northern Hemisphere (NH) [*Stein et al.*, 2014]. With an average CO lifetime of about 1–2 months, CO serves as a tracer of pollution emission and transport, and as a proxy for emissions and distributions of other species coemitted with CO that are not easily observed. The highest CO concentrations are found in the lowermost troposphere over urbanized regions in Asia, North America (and to a lesser extent in Europe), and over biomass burning regions mostly over the tropical rainforests and savanna grasslands in the Amazon, Central Africa, and Southeast Asia. Large CO enhancements are also observed during episodic fires in the NH summer (e.g., Russian fires in 2010). Understanding the trends in total column CO, which has shown a decrease of around 1%/year in the NH

[*Worden et al.*, 2013], has implications for greenhouse gases $CO_2$ and tropospheric $O_3$ (CO is a precursor) and $CH_4$ (less CO reduces $CH_4$ lifetime via OH).

Accurate spatiotemporal distribution of CO abundance is therefore important for both air quality and chemistry/climate. Observed abundance of CO is currently utilized in the evaluation of global chemistry and climate models, especially in representing emissions and transport of constituents and the oxidizing capacity of the troposphere. Based on observations, it has been shown that global models underestimate NH extratropical CO, which is attributed to the underestimation of surface emissions in the models [*Shindell et al.*, 2006]. Of all the tropospheric primary pollutants, CO is one of the most extensively observed species from space. Global monitoring of CO in the last two decades has been facilitated by the deployment of spaceborne instruments using nadir geometry to measure infrared radiances. One of the first nadir sounders that gave a global dense coverage with enhanced sensitivity to tropospheric CO is the Measurement Of Pollution In The Troposphere (MOPITT) instrument on the Terra mission (NASA) launched in late 1999. The new version of the MOPITT CO multispectral (thermal infrared (TIR) and near infrared (NIR)) retrievals [*Deeter et al.*, 2011] has enhanced surface sensitivity over many land regions, compared to TIR only retrievals and provides an improved estimate of CO near source locations. More recently, the Infrared Atmospheric Sounding Interferometer (IASI) instrument was launched in 2006 on board the first European meteorological polar-orbiting satellites, MetOp-A. IASI currently provides a much better spatial coverage of tropospheric CO, which is retrieved from measurements in the TIR [*Clerbaux et al.*, 2009]. A second instrument, mounted on the MetOp-B satellite, was recently launched in September 2012, while a third instrument is planned to be mounted on the MetOp-C satellite with the launch scheduled for 2018. Both MOPITT and IASI instruments provide extensive retrievals of total CO column and vertical profiles.

Over the last decade, several studies have performed global CO data assimilation of MOPITT and IASI retrievals as well as inverse modeling of CO sources. Data assimilation (DA) provides a systematic means to (a) integrate these satellite retrievals into chemistry/climate models (i.e., reanalysis) and (b) confront models with these data to gain insights on how to improve their predictive capability (i.e., better representation of sources, transport, and sinks). Data assimilation of MOPITT CO was initiated at the National Center for Atmospheric Research (NCAR) by *Lamarque et al.* [2004] using a suboptimal Kalman filter and the MOZART (Model for Ozone and Related chemical Tracers) chemical transport model (CTM). *Yudin et al.* [2004] used the same data assimilation system to optimize CO emissions in MOZART. Later, *Arellano et al.* [2007] assimilated MOPITT CO, in addition to meteorological conventional observations, in a chemistry/climate model (Community Earth System Model-Community Atmospheric Model with Chemistry (CESM-CAM-chem)) using the ensemble Kalman filter approach of the Data Assimilation Research Testbed (DART). Global MOPITT CO data assimilation started later over Europe with *Claeyman et al.* [2010] and *El Amraoui et al.* [2010] where assimilation was performed with a CTM using a 3-D variational data assimilation scheme. Recent studies such as *Jiang et al.* [2013] assimilated the new multispectral version of MOPITT CO retrievals to study the influence of vertical transport errors on inferred CO sources. Assimilation of IASI CO retrievals has also been performed in recent years. *Fortems-Cheiney et al.* [2009] used IASI and MOPITT CO retrievals separately at 700 hPa to estimate CO emissions. They showed in particular that the smaller vertical sensitivity of IASI (TIR-based) is compensated by its horizontal coverage. *Klonecki et al.* [2012] assimilated IASI CO total columns in a global CTM, and recently, *Inness et al.* [2013] presented an 8 year long reanalysis of atmospheric composition into a CTM that includes, among other sounders, assimilation of MOPITT and IASI CO total columns.

The first aim of this paper is to provide an extensive description and evaluation of the updated CESM-CAM-chem and DART chemical data assimilation system first used by *Arellano et al.* [2007]. A methodological aspect is provided throughout the paper in order to give useful insights to the ensemble-based chemical data assimilation community. To our knowledge, this is one of the first ensemble-based DA applications for which MOPITT CO profiles and IASI CO profiles are jointly assimilated with meteorological observations in a chemistry/climate model. The joint assimilation provides unique opportunities to elucidate the capability of these retrievals to constrain the global model given differences in spatiotemporal coverage and vertical sensitivities/resolution between MOPITT and IASI. The second aim of this paper is hence to define and describe the capabilities of each instrument to improve the modeled spatiotemporal distribution of CO and its associated emissions. Synergies of MOPITT CO and IASI CO in this joint assimilation will be discussed.

This paper is organized as follows: Section 2 describes in detail the MOPITT and IASI retrievals as well as the data assimilation setup. In particular, we describe and discuss observational characteristics of MOPITT and IASI CO

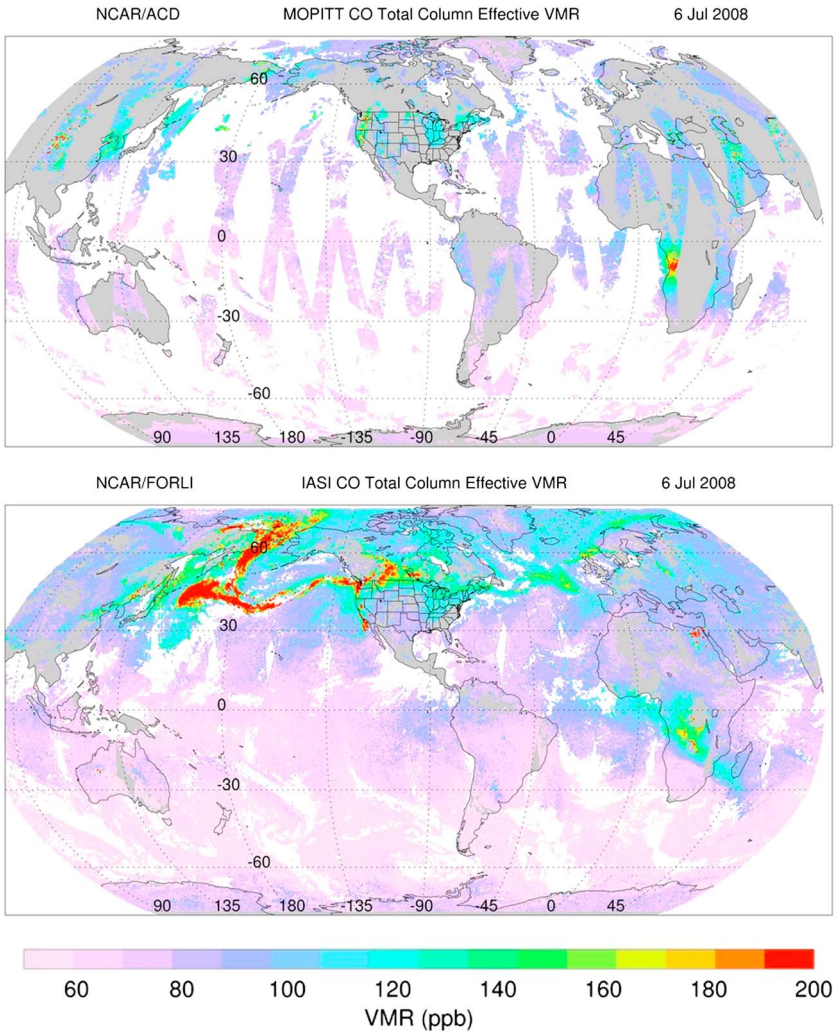


**Figure 1.** (top) MOPITT and (bottom) IASI footprints and total column effective VMR of CO (see text for details) for 6 July 2008.

profile retrievals in terms of sampling, horizontal coverage, and vertical sensitivities. This is followed by descriptions of DART and CAM-chem. Section 3 presents a description of the design and a discussion of results of the observing system experiments that we have carried out for this work. Section 4 provides a detailed evaluation against independent measurements and discussion of the contribution of each assimilated instrument in the model from the tropics to the arctic region. Section 5 gives the summary and conclusions of this paper.

## 2. Assimilation Setup

### 2.1. Low-Earth-Orbiter CO Observations

#### 2.1.1. MOPITT

The Measurement Of Pollution In The Troposphere (MOPITT) instrument is onboard the NASA Terra, which is a Sun-synchronous polar-orbiting satellite. With a swath width of 640 km perpendicular to the satellite track, MOPITT provides a near global coverage every 3–4 days with $22 \times 22\ km^2$ horizontal resolution. Figure 1 (top) shows the coverage of MOPITT on 6 July 2008. MOPITT is a gas-filter correlation radiometer (GFCR) measuring thermal infrared (TIR) and near-infrared (NIR) radiances in the absorption bands of CO and $CH_4$ [*Drummond et al.*, 2010]. In this paper, we use the V5J multispectral CO product as described in *Deeter et al.* [2011]. This is a relatively new CO retrieval using the TIR and NIR channels in MOPITT. These retrievals allow enhanced sensitivity in the lower troposphere in daytime observations over land. It should be noted, however, that this product exhibits relatively large random retrieval errors [*Deeter et al.*, 2013] (see section 2.1.3 for details)

compared to the TIR-only product. The MOPITT V5J product consists of a 10-layer CO profile (in volume mixing ratio or VMR) and total column (in molecules per square centimeter) retrievals. The profile consists of a floating surface level followed by 100 hPa thick layers from 900 hPa to 100 hPa. The retrieval method requires cloud-free observations and uses an algorithm based on optimal estimation approach as described by *Rodgers* [2000] with CO parameters in $\log_{10}$(VMR). The a priori error covariance matrix prescribed in the retrieval algorithm uses a variance of 30% at all levels and an error vertical correlation length of 100 hPa [*Deeter et al.*, 2010]. It also uses the variable a priori CO profile from the MOZART-4 (Model for Ozone and Related chemical Tracers, version 4) [*Emmons et al.*, 2010] climatology. The retrieval product also includes key diagnostics such as the averaging kernel and retrieval error covariance matrices. The averaging kernel expresses the sensitivity of a given layer of the retrieved profile relative to the true CO state. As such, the retrieval equation can be expressed as follows:

$$\log_{10} y_{\text{ret}}^{\text{MOPITT}} = \boldsymbol{A}^{\text{MOPITT}} \log_{10} y_{\text{true}} + \left(I - \boldsymbol{A}^{\text{MOPITT}}\right) \log_{10} y_{\text{apr}}^{\text{MOPITT}} \quad (1)$$

where $y_{\text{ret}}^{\text{MOPITT}}$ is the retrieved profile, $y_{\text{true}}$ is the true CO state, $y_{\text{apr}}^{\text{MOPITT}}$ is the a priori profile, $\boldsymbol{A}^{\text{MOPITT}}$ is the MOPITT averaging kernel matrix, and $I$ is an identity matrix. Please refer to section 2.2.4 for description of the methodology to take into account $\boldsymbol{A}$ in the construction of the observation operator for MOPITT CO assimilation. In the current data assimilation setup, we only consider the error variance (diagonal elements of the retrieval error covariance matrix) as a first-order estimate of the retrieved error ($\epsilon_{\text{ret}}^{\text{MOPITT}}$). Similar approach has been employed by recent state–of-the-art assimilation studies on CO partial column or profile, such as *El Amraoui et al.* [2014] where they used the diagonal elements of the covariance matrix and *Jiang et al.* [2013] where they specified the error covariance as a factor (e.g., 20%) of the retrieved profile values. Accounting for the off-diagonal elements of the error covariance matrix in the ensemble Kalman filter scheme is an ongoing work that requires robust testing and algorithm development, which will be presented in a further study.

The MOPITT CO V5J product has been evaluated against independent measurements [*Deeter et al.*, 2012]. In particular, it has been evaluated over the Continental United States (CONUS) using both in situ vertical profiles and NOAA ground-based measurements. Validation results based on the in situ profiles (smoothed by the MOPITT retrieval a priori profile and averaging kernel) indicate that retrieval biases from 400 hPa to surface levels are less that ±5%. However, a persistent positive bias of 14% is observed on the upper tropospheric levels [*Deeter et al.*, 2013]. For this reason, we only use the levels below 300 hPa. Although a later version of the multispectral product is currently available (MOPITT V6J [*Deeter et al.*, 2014]) with a corrected bias in the upper troposphere (3.4%), this product exhibits a larger bias near the surface (8.9%) and consequently was not appropriate for use in this study.

#### 2.1.2. IASI

The Infrared Atmospheric Sounding Interferometer (IASI) is one of the instruments onboard MetOp-A, which is also a polar-orbiting satellite. Due to a large swath width of 2200 km perpendicular to the satellite track, IASI provides global coverage in 2 days. Figure 1 (bottom) show the coverage of IASI on 6 July 2008. The horizontal resolution is $12 \times 12\ \text{km}^2$ circular footprint on the ground. IASI is a Fourier transform spectrometer (FTS) that measures infrared radiances. The CO IASI data are retrieved using the Fast Optimal Retrievals on Layers for IASI (FORLI-CO) retrieval code [*Hurtmans et al.*, 2012]. The FORLI algorithm retrieves CO profiles on 19 layer under cloud-free conditions. The retrieval method uses the same optimal estimation scheme described by *Rodgers* [2000]. The a priori information used in the retrieval is a constant single profile and an error covariance matrix that are constructed using a database of observation (Measurement of Ozone and Water Vapor by Airbus In-service Aircraft (MOZAIC)/In-service Aircraft for a Global Observing System flights and Atmospheric Chemistry Experiment-FTS retrievals [*Clerbaux et al.*, 2008]) complemented with global model (Laboratoire de Météorologie Dynamique-INteraction with Chemistry and Aerosols) information to account for both polluted and background conditions [*Turquety et al.*, 2009].

The IASI CO product consists of retrieved VMR profiles with 19 altitude levels corresponding to vertical layers of 1 km thickness starting from the surface to 18 km. The last level represents a layer from 18 km to the top of the atmosphere. Like MOPITT, each profile has an associated retrieval error covariance matrix and an averaging kernel matrix. The retrieval equation can be expressed as follows:

$$y_{\text{ret}}^{\text{IASI}} = \boldsymbol{A}^{\text{IASI}} y_{\text{true}} + \left(I - \boldsymbol{A}^{\text{IASI}}\right) y_{\text{apr}}^{\text{IASI}} \quad (2)$$

where $y_{\text{ret}}^{\text{IASI}}$ is the retrieved profile, $y_{\text{true}}$ is the true CO state, $y_{\text{apr}}^{\text{IASI}}$ is the a priori CO profile, $\boldsymbol{A}^{\text{IASI}}$ is the IASI averaging kernel matrix, and $I$ is an identity matrix. As with MOPITT, we only consider the error variance

**Table 1.** Key Differences Between IASI and MOPITT Sampling and Error Characteristics (Statistics Are Computed for All Scenes: Night and Day Times, Sea and Land Surfaces)

| | Obs/Day | Obs/Day | | | |
|---|---|---|---|---|---|
| Data | Raw Data | After Preprocessing | Global Coverage | Average Area of $\boldsymbol{A}_i$ | Average Relative Error |
| MOPITT | 10 levels<br>$10^5$ footprints | 7 levels<br>$6 \times 10^3$ footprints | 3–4 days | 0.73 | 20–30% |
| IASI | 19 levels<br>$4 \times 10^5$ footprints | 10 levels<br>$2 \times 10^4$ footprints | 2 days | 1.04 | 15–25% |

(diagonal elements of the retrieval error covariance matrix) and consider a retrieved error profile $\epsilon_{\text{ret}}^{\text{IASI}}$ in the data assimilation.

The IASI CO FORLI product has been evaluated against independent measurements in several recent studies. *De Wachter et al.* [2012] used MOZAIC flights and *Kerzenmacher et al.* [2012] used Network for the Detection of Atmospheric Composition Change Fourier transform infrared (NDACC FTIR) sites for validation. The IASI CO FORLI retrievals show biases no higher than 13% compared to MOZAIC flights. Comparisons with NDACC FTIR sites and IASI CO total columns showed that there is no significant bias on a global scale.

#### 2.1.3. Differences Between MOPITT and IASI

Table 1 summarizes some of the differences between MOPITT and IASI. One of the most obvious differences is the number of observations provided and their coverage. Both instruments are on low Earth orbit satellites with Sun-synchronous orbits. MOPITT on TERRA has a descending (ascending) node of 10:30 A.M. (10:30 P.M.), while IASI on MetOp-A has a descending (ascending) node of 9:30 A.M. (9:30 P.M). The IASI measurement swath allows nearly global coverage in 2 days, while the MOPITT swath provides global coverage in 3–4 days [*Drummond et al.*, 2010]. Figure 1 shows daily total CO column retrieved by IASI and MOPITT during 6 July 2008 (both night and day) as an example. IASI swaths of contiguous ascending (or descending) tracks almost overlap near the equator. On the other hand, the MOPITT swaths are narrower leaving gaps of unmonitored regions within a given day. These spatial and temporal variations in data coverage limit the ability for a given sounder to observe the highly variable nature of the tropospheric CO distribution. A higher coverage obviously increases the chances to capture large gradients of pollution and to track its transport downwind of source regions. In addition to horizontal spatial coverage, MOPITT- and IASI-collocated CO total column values exhibit differences due to instrument design (e.g., correlation radiometer versus interferometer with subsequent differences in performance, e.g., spectral resolution and signal to noise), possible biases, retrieval algorithms that use different a priori information for CO profiles and error covariance matrices and hence different instrument sensitivity.

Figure 2 shows examples of averaging kernels to demonstrate the different characteristics of $A$ for each instrument for two observation types and provide degrees of freedom for signal (DFS). Following *Rodgers* [2000], the DFS is calculated as the trace of $A$ and quantify the numbers degrees of freedom of a measurement are related to signal. The averaging kernels in Figure 2 were collocated in the same $1° \times 1°$ latitude longitude box and in the same 6 h time window, and IASI averaging kernel have been regridded on MOPITT vertical grid (see methods provided by *Von Clarmann and Grabowski* [2007] and *Zhang et al.* [2010]). The first example is over land in daytime with good thermal contrast conditions, and the second is over the Pacific Ocean at night with less favorable thermal contrast conditions. These examples show typical shapes of averaging kernel that can be found in the satellite CO data. The daytime land averaging kernels (Figure 2, top row) show higher DFS and enhanced sensitivity toward the surface. This is especially the case for MOPITT data since the V5J product uses TIR/NIR retrieval that allows a peak of sensitivity at the surface. For IASI retrievals, the lowest peak of sensitivity is located around 800 hPa in addition to significant sensitivity to the upper tropospheric levels. Ocean averaging kernels (Figure 2, bottom row) are more representative of the rest of the measured conditions, i.e., oceans and/or nighttime that are 85% of observations. These cases have lower DFS than daytime/land, with most of the sensitivity located in the middle and upper troposphere. For the ocean and/or night observations, MOPITT retrievals use only TIR radiances since NIR radiances are only significant for daytime/land. Because of biased MOPITT data in the upper troposphere we did not assimilate the levels from 100 hPa to 300 hPa (see section 2.1.1). The remaining MOPITT averaging kernel profiles over oceans are flat and have low values of sensitivity over the entire troposphere. Conversely, ocean IASI

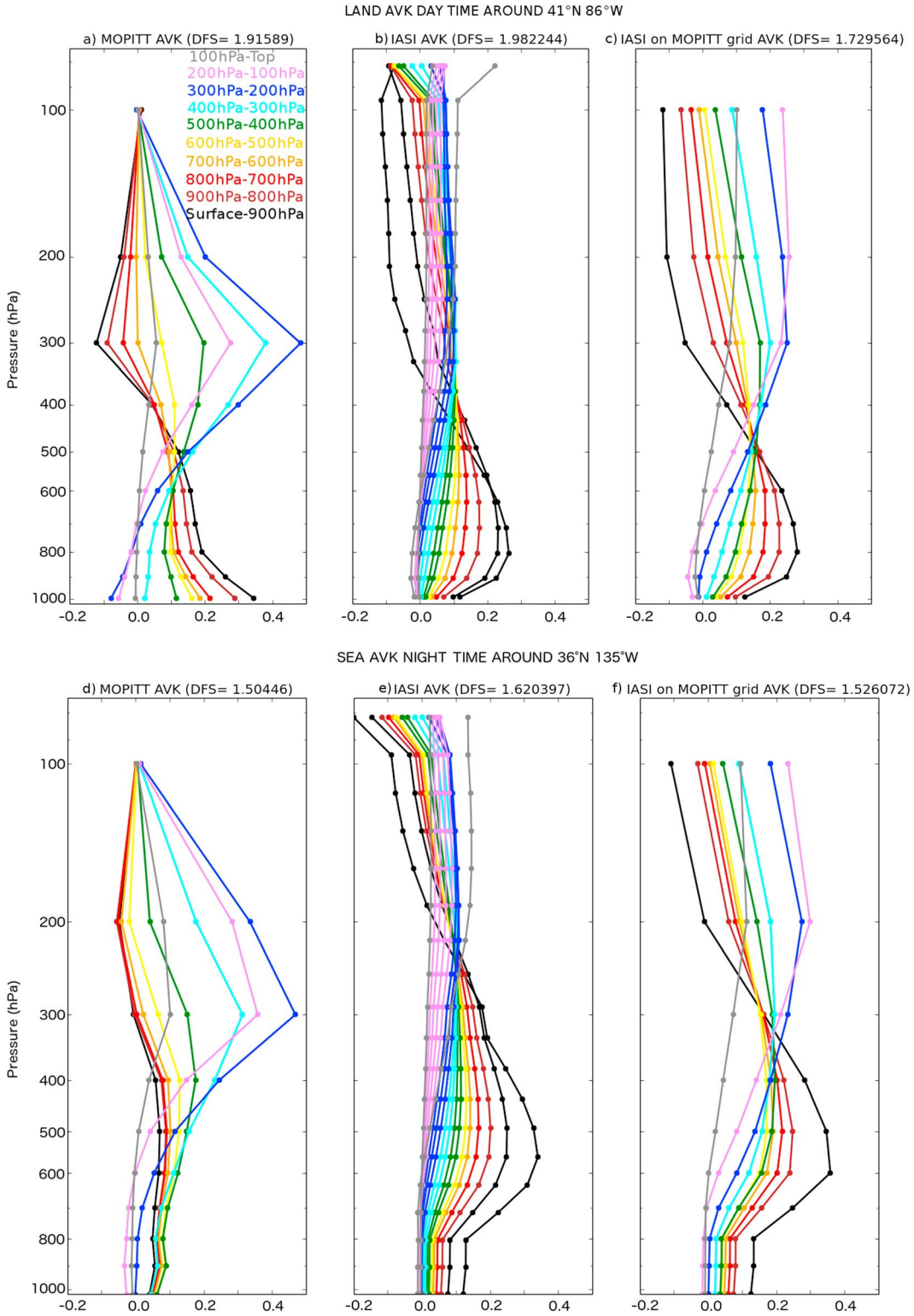


**Figure 2.** (left column) Collocated MOPITT and (middle column) IASI averaging kernel matrices (top row) for land/day conditions and (bottom row) for ocean/night conditions. The right column represents the corresponding IASI averaging kernels gridded to the MOPITT vertical resolution.

averaging kernels still show a peak of sensitivity that is switched from 800 hPa to 600 hPa as well as sensitivity to the upper tropospheric levels.

Differences in averaging kernel functions from the MOPITT and IASI instruments can be attributed to instrumental and retrieval factors. First, the multispectral dimension (TIR + NIR) of MOPITT allows a peak of sensitivity at the surface during daytime [*Worden et al.*, 2010] that a TIR-only retrieval (i.e., IASI) can produce only under relatively rare conditions of very high thermal contrast [*Boynard et al.*, 2014], while the IASI instrument has higher TIR sensitivity than MOPITT [*George et al.*, 2015]. Second, the MOPITT and IASI retrieval algorithms use different state vectors, a priori and noise covariance matrices. Some of the differences in DFS between MOPITT and IASI are due to how surface emissivity and water vapor are treated in the state vector (the MOPITT algorithm assumes a fixed water vapor profile from NOAA/National Centers for Environmental Prediction (NCEP) but retrieves emissivity simultaneously with CO while IASI uses a fixed emissivity but adjusts the water vapor amount). Another difference in retrievals is in the covariance where the IASI a priori covariance includes stronger off-diagonal correlations than MOPITT. Differences in the retrieval a priori covariance error matrix in the optimal estimation retrieval can result in different averaging kernel functions (i.e., DFS and averaging kernel row areas, see Table 1) and hence different retrieval errors for the same radiance measurements [see *Rodgers*, 2000] (section 2.6). However, by applying the IASI a priori covariance and profile to retrievals with MOPITT data, it appears that instrument differences, such as measurement type (GFCR versus FTS) and noise, and the different parameters in the state vector outweigh the differences due to a priori covariance in the comparison of averaging kernels [*George et al.*, 2015].

Because we did not assimilate the MOPITT level profiles from 100 hPa to 300 hPa, MOPITT and IASI DFS are not straightforwardly comparable. In our current data assimilation setup each retrieved level is assimilated as an observation. For those reasons we also use the area of $A_i$ as a metric of sensitivity. Following *Rodgers* [2000], the area of $A_i$ (sum of the $i$th row of $A$) is found to be approximately unity at levels where the retrieval is most sensitive and, in general, can be thought of as a rough measure of the fraction of the retrieval that comes from the data, rather than the a priori. On a global average for all retrieval levels and taking night and day values, IASI exhibits an area that is around unity (1.03), while MOPITT shows a lower area of about 0.73 (see Table 1). Results would be higher for MOPITT if only land and day retrievals were taken for the calculation, which are the scenes that benefit the TIR/NIR combination with enhanced sensitivity at the surface. Night and day MOPITT and IASI measurements are assimilated.

### 2.2. Data Assimilation System

#### 2.2.1. CESM-CAM-chem

We use the National Center for Atmospheric Research (NCAR) Community Earth System Model (CESM) [*Lamarque et al.*, 2012] version 1.1.1 as the model component of the data assimilation system. This is a coupled climate/chemistry/land/ocean/ice model for simulating the Earth's climate system. In this study, we used the F_2000_MOZMAM_CN compset (all updates and bug fixes have been added as described in *Tilmes et al.* [2015]), which simulates only the atmosphere and land including their interactions while employing a data ocean (sea surface temperature mode) and prescribed sea ice. The atmosphere model is the Community Atmospheric Model with Chemistry (CAM-chem) version 5 with online meteorology (using CAM5 physics [*Conley et al.*, 2012]) and online full chemistry scheme (MOZART-4 tropospheric chemistry). The MOZART-4 tropospheric scheme has been described and evaluated by *Emmons et al.* [2010]. The standard MOZART mechanism includes 85 gas-phase species, 12 bulk aerosol compounds, 39 photolysis, and 157 gas-phase reactions for the troposphere, while the chemistry in stratosphere (between 50 hPa and the top of the model) is prescribed using a climatology. The CAM-chem component of CESM has been described and evaluated by *Lamarque et al.* [2012]. CAM-chem borrows heavily from MOZART-4. In particular, many of the parameterizations needed to represent atmospheric chemistry in a global model are adapted or expanded from their equivalents in MOZART-4. In this paper, we use a model resolution of 2.5° longitude by 1.9° latitude with 30 vertical levels covering the troposphere and the lower stratosphere. The vertical layers range from the surface to 4 hPa, with 8 levels representing the planetary boundary layer and 19 tropospheric levels.

Simulations of CO concentrations in the atmosphere are calculated by a continuity equation consisting of the following terms: direct emission and chemical production by VOC oxidation, loss through CO-OH reaction, and dry deposition as well as redistribution through transport (e.g., advection, convection, and turbulent mixing). *Lamarque et al.* [2012] and *Tilmes et al.* [2015] showed that the modeled CO distribution in the high NH

latitudes is underestimated when compared to surface, aircraft, and satellite observations, indicating an overestimate of the CO loss by OH or underestimate of its emissions or chemical production. *Monks et al.* [2015] diagnosed the methane lifetime as an indication of the OH abundance and found that CAM-chem has higher OH among other models. The anthropogenic emissions are based on the Atmospheric Chemistry and Climate Model Intercomparison Project historical emissions (1960–2000) and Representative Concentration Pathway 8.5 future scenario emissions [*Lamarque et al.*, 2010]. Biomass burning emissions are provided by the Fire Inventory from NCAR version 1.5 (FINNv1.5 [*Wiedinmyer et al.*, 2011]). Biogenic emissions are generated offline using the global Model of Emissions of Gases and Aerosols from Nature (MEGAN v2.1) [*Guenther et al.*, 2012]. Daily emissions from MEGAN and FINN are monthly averaged and are emitted in the surface level. Using monthly average for fire emission inventory is likely a source of error knowing that fires have daily evolving signatures. Following *Gaubert et al.* [2014], an ensemble of perturbed states is used to represent errors in emissions using an additive noise that is randomly sampled from a pseudo-normal distribution [*Evensen*, 2003, Appendix E]. Here we use a fixed standard deviation and horizontal correlation length. The same noise is applied over time with a spatial correlation length of 2000 km, and for all source types (i.e., biogenic, anthropogenic, oceanic, and biomass burning). This correlation length has been chosen based on qualitative inspection of spatiotemporal patterns of emissions around the globe. We use a standard deviation of 40% for CO and 30% for nonmethane volatile organic compounds, HCN, $CH_3CN$, NO, and $NH_3$. This is in the range of previous ensemble-based chemical data assimilation studies [*Miyazaki et al.*, 2012].

#### 2.2.2. Data Assimilation Research Test Bed

The Data Assimilation Research Testbed (DART) [*Anderson et al.*, 2009] is a community data assimilation software package that has been developed since 2002 at NCAR. DART is based on the ensemble Kalman filter (EnKF) technique originally introduced by *Evensen* [1994]. This software has been carefully designed to provide high modularity that allows an easy interface for a variety of models. It facilitates ensemble-based data assimilation (DA) without needing to construct adjoints of the model and observation operators as in the case of variational-based DA.

The EnKF scheme is basically an ensemble of Kalman filters (KF). Following Kalman theory, the EnKF recursively integrate observations into the forecast of a numerical model of the dynamical system (in our case, CAM-Chem). The main goal is to produce an improved estimate or analysis of the mean state (in our case the physical and chemical state of the atmosphere). Instead of calculating (e.g., extended KF) or prescribing (e.g., Optimal Interpolation or 3D-Var) the associated error covariance of the mean forecast state, the EnKF scheme carries out an ensemble of model forecasts through addition of representative observation and model perturbations and use the resulting ensemble statistics (covariance) to represent flow-dependent errors relative to the ensemble mean. This approach has been shown to converge to a Kalman filter for large ensemble sizes *Evensen* [1994], without needing to calculate the evolution of the error covariances, which otherwise is impractical to implement for large geophysical systems. In practice, small ensemble sizes are used for computational expediency.

DART mainly uses a "deterministic" variant of EnKF called ensemble adjustment Kalman filter (EAKF) introduced by *Anderson* [2001]. It ensures that both posterior (or analysis) mean (i.e., expected value of the ensemble) and the posterior spread (i.e., standard deviation of the ensemble) are consistent with Kalman filter theory. Since DART uses small ensemble sizes, it also employs (like all EnKF variants) several approximations. In particular, it uses covariance inflation and localization to minimize degeneracy in covariance matrices, errors in sampling and filter divergence (please refer to *Anderson* [2009 and references therein] for more discussion on these approximations). For the purpose of this study, we describe in section 2.2.3 the details of the filter procedure including inflation and localization schemes employed in this work.

We use a 30-member ensemble over a 6 hourly assimilation window for all assimilation experiments that we carried out. This choice is based on the work of *Arellano et al.* [2007], which showed good results using a 20-member ensemble with a 6 h window using DART and CAM-chem CO data assimilation. As with *Arellano et al.* [2007], the current DA configuration assimilates meteorology. NOAA/NCEP conventional meteorological observations of surface pressure, air temperature, winds, and specific humidity (including land surface, marine surface, radiosonde, pibal, and aircraft reports from the Global Telecommunications System, profiler and U.S. radar-derived winds, Special Sensor Microwave Imager oceanic winds and total column water retrievals, and satellite wind data from the National Environmental Satellite Data and Information Service, http://rda.ucar.edu/datasets/ds337.0/) are assimilated in CESM-CAM-chem/DART. Note that no satellite radiance assimilation is performed. A detailed

evaluation of the performance of the meteorological analysis can be found in the supporting information associated to this paper. We refer the reader to *Raeder et al.* [2012] for the full description, extensive validation of meteorological DA in CAM/DART.

#### 2.2.3. Filter Procedure

In this section, we discuss the algorithm of the EAKF scheme briefly described above. Readers who are already familiar with this algorithm may move forward to section 3. For notation purposes, we represent $y$ and $x$ as variables in observation space and model state space, respectively. The assimilation cycle begins with a 6 h model advance for each $j$th ensemble member to produce an ensemble forecast (prior) of the model state ($x_j^f$). These forecasts are then transformed into expected observations ($y_{m,j}^f$) using a unique observation operator $h$ (see section 2.2.4) for a given observation type: i.e., $y_{m,j}^f = h\left(x_j^f\right)$. One can then compute the associated ensemble forecast mean $\overline{y}_m^f$ and ensemble spread $\sigma_m^f$ (i.e., sample standard deviation) of the model in the observation space. Prior to adjusting $y_{m,j}^f$, $\overline{y}_m^f$, and $\sigma_m^f$ to match a given observation $y_o$ with its associated error $\sigma_o$, we apply our first approximation by increasing the ensemble spread of the model state in order to minimize filter divergence due to insufficient variance. In particular, we apply an inflation factor $\lambda$ to $x_j^f$ in the following manner:

$$x_j^f = \sqrt{\lambda}\left(x_j^f - \overline{x}^f\right) + \overline{x}^f \tag{3}$$

where $\overline{x}^f$ is the ensemble mean. The inflation factor is computed such that the total spread is about the distance between the ensemble mean and the observation, i.e.,

$$y_o - \overline{y}_m^f = \sqrt{\lambda\left(\sigma_m^f\right)^2 + \left(\sigma_o\right)^2} \tag{4}$$

Here we use an adaptive inflation as described by *Anderson* [2009] and implemented for example in *Raeder et al.* [2012]. We note that inflation increases the spread of the model states (and expected observations) while preserving the error covariances.

To adjust each ensemble member $y_{m,j}^f$, we use a local least squares framework [*Anderson*, 2003] to compute an analysis $y_{m,j}^a$ such that the ensemble mean $\overline{y}_m^f$ closely matches with $y_o$ and that the ensemble spread $\sigma_m^f$ is reduced consistent with $\sigma_o$, in essence satisfying the analysis equations of a Kalman filter. The analysis in observation space, which is the first step in the two-step framework described by *Anderson* [2003], is given by

$$y_{m,j}^a = \left[\sqrt{\frac{{\sigma_o}^2}{{\sigma_o}^2 + {\sigma_m^f}2}}\right]\left[y_{m,j}^f - \overline{y}_m^f\right] + \frac{\left[\frac{\overline{y}_m^f}{{\sigma_m^f}2} + \frac{y_o}{{\sigma_o}^2}\right]}{\left[\frac{1}{{\sigma_m^f}2} + \frac{1}{{\sigma_o}^2}\right]} \tag{5}$$

and the corresponding increment in observation space is

$$\Delta y_{m,j} = y_{m,j}^a - y_{m,j}^f \tag{6}$$

This is a deterministic approach to adjust the ensemble members, which differentiates EAKF (square-root filters) with other stochastic variants of EnKF. Note that the increment is a function of the error variances, ${\sigma_o}^2$ and ${\sigma_m^f}2$. The next step is to update the model states. The analysis increment $\Delta x_j$ for each ensemble member in the model space is computed as the product of $\Delta y_{m,j}$ and a linear regression coefficient calculated as the covariance of $x^f$ and $y_m^f$ across the ensemble, $\sigma\left(x^f, y_m^f\right)$, divided by the variance $\left(\sigma_m^f\right)^2$ [*Anderson*, 2003]. These two steps constitute the analysis equation of the mean state in a Kalman filter. The forecast error covariance is estimated via the ensemble forecasts as a result of model perturbations (e.g., *Buehner* [2005], and for this work please see section 2.2.1), rather than typical approximations such as the National Meteorological Center method using lagged forecasts [e.g., *Parrish and Derber*, 1992] or methods based on innovation statistics [e.g., *Desroziers et al.*, 2005].

Since a small ensemble size is typically used, we apply a covariance localization function $\alpha$ to minimize sampling error. In effect, the analysis increments described above is "localized" across neighboring model states and dampened with increasing distance from observation location. The final expression of the increment is as follows:

$$\Delta x_j = \alpha \frac{\sigma\left(x^f, y_m^f\right)}{\left(\sigma_m^f\right)^2} \Delta y_{m,j} \tag{7}$$

The localization function in this study is made up of two components. First, we multiply a Gaspari-Cohn (GC) correlation function [*Gaspari and Cohn*, 1999] to the analysis increment. This function effectively limits the increments within a local volume around the location of the observation. The GC function has basically a Gaussian shape with values starting from 1 (over the observation location) and tapering off isotropically to 0 with increasing distance from the observation location. The GC function is characterized by a half-width parameter, which defines the distance at which the GC value is 0.5. In assimilating meteorological observations, we use the half-width parameter of the GC function to be 0.2 radians in the horizontal (~1200 km) and 400 hPa in the vertical, as has been chosen in *Raeder et al.* [2012]. For chemistry (CO), we reduce the half-width to 0.1 rad in the horizontal and 200 hPa on the vertical. The choice of reducing the cutoff is justified by high horizontal satellite data sampling and strong horizontal and vertical gradients in the CO fields, which can lead to spurious increments for low ensemble sizes as in the case here. Sensitivity tests on these length scales ranging from 0.1 to 0.2 rad in the horizontal and/or from 100 hPa to 200 hPa in the vertical (not shown) did not significantly change the results presented here. To locate the center (maximum) of the GC function in the vertical (for CO retrievals), we use the vertical location of the maximum value of the retrieval averaging kernel profile. It is important to keep in mind that the length scales for the GC function used here for localization do not represent the length scales of the forecast error covariances that are typically defined a priori in suboptimal Kalman filters. As mentioned above, the error covariance in EAKF is defined by the ensemble statistics. These are not necessarily isotropic (i.e., depends only on spatial distance). In fact, the error covariance typically show flow-dependent structures, which are more representative of model forecast errors due, for example, to errors in representing emissions, transport, and/or removal mechanisms. The GC function does not alter this structure but only localizes the error covariance.

The second component of the localization scheme pertains to localizing the impact of certain observation types to a group of model state variables. This is called state variable localization. In this work, observations of temperature, winds, surface pressure, and specific humidity will only impact meteorological state variables (e.g., temperature). For example, the increment $\Delta y_{m,j}(T)$ from a temperature observation can be used to produce an analysis increment of model states other than temperature (e.g., $\Delta x_j(U, V)$ of horizontal wind) whenever there is significant local sensitivity (i.e., regression coefficient is nonzero in equation (5)). For this study, we localize the impact of increments due to CO observations to only influence the model CO states. Under this current DA framework, there is, however, an opportunity to investigate the potential constraints of CO observations on other state variables (i.e., other chemical or meteorological variables). This topic of chemical/dynamic balance is important and will be discussed in a further study.

#### 2.2.4. Assimilation of Full Nadir CO Profiles: Design of the Observation Operator

Observation operators for MOPITT and IASI have been implemented using the retrieval equation similar to

$$y_{\text{ret}}^{\text{CAM}} = \boldsymbol{A}^{\text{SAT}}\, y^{\text{CAM}} + \left(I - \boldsymbol{A}^{\text{SAT}}\right) y_{\text{apr}}^{\text{SAT}} \tag{8.1}$$

where $y_{\text{apr}}^{\text{SAT}}$ and $\boldsymbol{A}^{\text{SAT}}$ are the a priori CO profile and averaging kernel matrix from either satellite product (MOPITT or IASI), respectively; $y^{\text{CAM}}$ is the CO profile from the original CAM-chem profile $x^{\text{CAM}}$ on the retrieval grid, and $y_{\text{ret}}^{\text{CAM}}$ is the "smoothed" CAM-chem profile that is directly comparable to the IASI or MOPITT retrieved profiles ($y_{\text{ret}}^{\text{IASI}}$, $y_{\text{ret}}^{\text{MOPITT}}$). Note that the MOPITT observation operator is in log VMR space (see section 2.1.1). We apply the exponential function to $y_{\text{ret}}^{\text{CAM}}$ in equation (1) in the case of MOPITT data to transform the smoothed model profile (in $\log_{10}$ VMR space) to VMR space during the filter procedure. In the case of MOPITT the observation operator is then:

$$y_{\text{ret}}^{\text{CAM}} = 10^{\left(\boldsymbol{A}^{SAT}\ \log_{10} y^{\text{CAM}} + \left(I - \boldsymbol{A}^{\text{SAT}}\right)\ \log_{10} y_{\text{apr}}^{\text{SAT}}\right)} \tag{8.2}$$

It has been shown (see Figure S1 in the supporting information) that equation (8.2) gives similar results to equation (8.1), and hence, equation (8.2) (equation (1)) can be approximated to equation (8.1) (equation (2)). The error associated to this approximation is mostly below 10% of the retrieval error, hence not affecting significantly the data assimilation results. Adding the retrieval a priori $\left(I - \boldsymbol{A}^{\text{SAT}}\right) y_{\text{apr}}^{\text{SAT}}$ on the observation operator removes the retrieval a priori contribution in the innovation vector. By combining equations (8.1) and (2) the innovation is then

$$y_o - y_{\text{ret}}^{\text{CAM}} = \boldsymbol{A}^{\text{SAT}} \left(y_{\text{true}} - y^{\text{CAM}}\right) \tag{9}$$

Consider $j$ retrieval levels, where each retrieval level corresponds to a partial column with $N$ model levels ($N \geq 1$). We can define a model partial column $z_i^{\mathrm{CAM}}$ for the $i$th given model level as follows:

$$z_i^{\mathrm{CAM}} = \frac{\Delta P_i \mathcal{N}_a}{g M_{\mathrm{CO}}} x_i^{\mathrm{CAM}} \tag{10}$$

where $\Delta P_i$ is the pressure thickness of the model layer, $\mathcal{N}_a$ is the Avogadro's number, $g$ is the acceleration of gravity, and $M_{\mathrm{CO}}$ is the molecular weight of CO. A model partial column on the retrieval grid will then be

$$z_j^{\mathrm{CAM/SAT}} = \sum_{i=1}^{N} z_i^{\mathrm{CAM}} \tag{11}$$

By transforming a partial column to VMR one would do

$$y_j^{\mathrm{CAM}} = \frac{g M_{\mathrm{CO}}}{\Delta P_i \mathcal{N}_a} z_j^{\mathrm{CAM/SAT}} \tag{12}$$

By replacing $z_j^{\mathrm{CAM/SAT}}$ using the equations above, the pseudo-VMR calculation on the retrieval grid is reduced to the following weighted mean where the weights are the associated model layer pressure thickness. In a given retrieval layer consider model layers ranging from $a$ to $b$:

$$y_j^{\mathrm{CAM}} = \sum_{i=a}^{b} \frac{\Delta P_i}{\sum_{i=a}^{b} \Delta P_i} x_i^{\mathrm{CAM}} \tag{13}$$

For model layers that are in between two retrieval layers, bottom (top) model layer pressure needs to be replaced by the bottom (top) retrieved layer pressure for exact calculation. Each value of the retrieved profile is then assimilated sequentially during the filter procedure. For straightforward comparison (see section 2.1.3) and data compression purposes, we transformed IASI CO to match the vertical grid of MOPITT (i.e., the number of profile values is reduced from 19 to 10; see Figure 2 and methods provided by *Von Clarmann and Grabowski* [2007] and *Zhang et al.* [2010]). Because there is more than one measurement per model grid box and per assimilation window from either MOPITT or IASI, we also compute superobservations to match the horizontal resolution between MOPITT (22 km), IASI (12 km), and CAM-chem (2.5° × 1.9° i.e., around 200 km). See Appendix A for the superobservation procedure.

## 3. Observing System Experiments

### 3.1. Experiment Design and Implementation

#### 3.1.1. Spin-Up and Control Run

CAM-chem has been spun-up from 1 January 2006 to 1 April 2008 with unperturbed emissions starting from a climatological state [*Lamarque et al.*, 2012]. A 2 month meteorology-only assimilation is then performed starting from 1 April 2008 using a 30-member ensemble. For this run, we used perturbed CO emissions (as described in section 2.2.1) in order to generate a reasonable CO ensemble spread (CO ensemble spin-up) while constraining modeled meteorology. Temperature is initially perturbed with a random noise of 0.5 K in order to initiate the assimilation cycling procedure (see section 2.2.3). CO is carried along in the ensemble model run and as part of the state vector. This setup generates an ensemble spread in meteorological variables and also in CO since each ensemble member is driven in the model run (forecast) by perturbed meteorology (including inflation) and CO emissions. For this setup, CO is not statistically influenced (in the analysis step) by the meteorological observations assimilated in CAM-chem. Subsequent meteorology-only assimilation is then carried out after this 2 month CO ensemble spin-up, starting 1 June 2008. We refer to this subsequent assimilation as our control run (CR). Table 2 gives a summary of all the experiments performed for the study.

We use the same meteorological DA setup as described and validated by *Raeder et al.* [2012] and similar conventional observations as used for the (National Center for Environmental Prediction) NCEP-NCAR reanalyzes. We show in Figure 3 key assimilation diagnostics for the first month of CO ensemble spin-up. In particular, we show time series statistics of observation minus ensemble mean forecast (OmF) and observation minus ensemble mean analysis (OmA) for temperature and wind to highlight successful meteorological assimilation for the spin-up and subsequent CR. Here the OmA is always smaller than OmF, showing that the assimilation (analysis) is effective in bringing the model closer to observations for each 6-hourly analysis cycle. Also, the

**Table 2.** Summary of Experiments

| | Meteorology | MOPITT CO | IASI CO |
|---|---|---|---|
| Experiment | Assimilation | Assimilation | Assimilation |
| CR: Control run | Yes | No | No |
| MR: MOPITT assimilation run | Yes | Yes | No |
| IR: IASI assimilation run | Yes | No | Yes |
| DR: Double assimilation run | Yes | Yes | Yes |

OmF and OmA show a general decreasing trend over time, suggesting improvements in the model forecast with data assimilation. The bottom plots of Figure 3 also show the ratios of OmF and the total spread, which is expressed as the square root of the sum of ensemble variance (including inflation) and observation error variance (please see section 2.2.3 for details on the error variances). This metric, which is also called Reduced Centered Random Variable (RCRV) [*Candille et al.*, 2007], provides a measure of the agreement of the ensemble spread and observational error with the amplitude of the forecast error. The second moment of the RCRV (root-mean-square (RMS) of RCRV) measure the agreement of the ensemble spread and the specified error with the observed amplitude of the forecast error. RMS of RCRV should converge to 1 after the spin-up. For CR, we find that meteorology needs around a week to spin-up. The OmF and OmA stabilize around a low threshold value and RCRV stays close to 1 after spin-up.

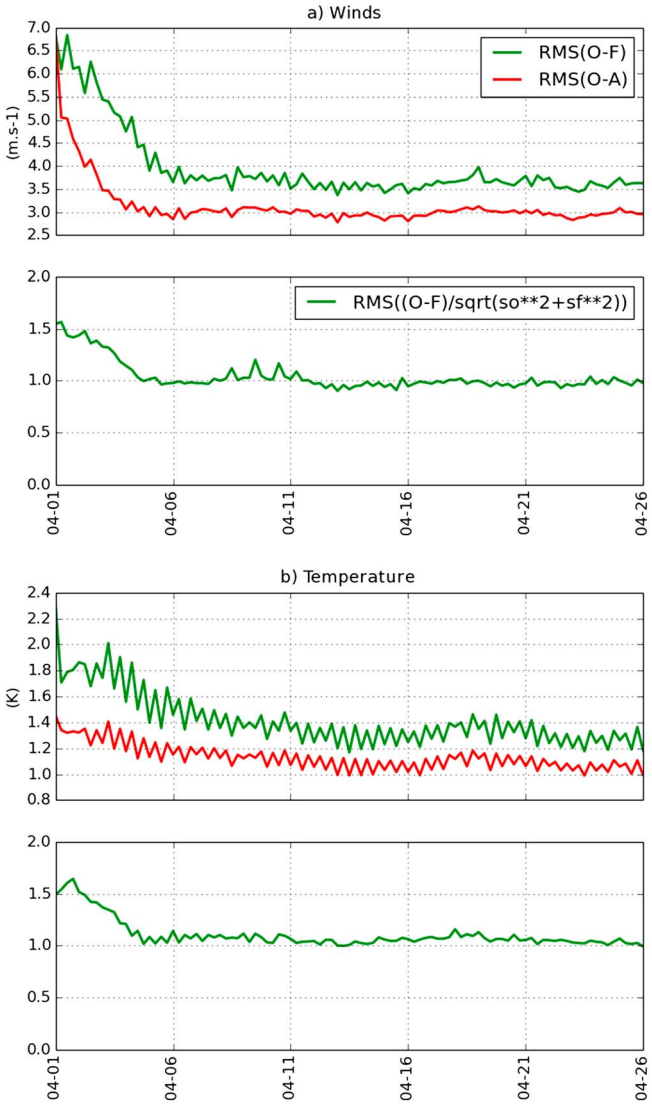


**Figure 3.** (top plots) Six-hourly RMS of observation minus forecast (OmF, green lines) and observation minus analysis (OmA, red lines). (bottom plots) RMS of RCRV for (a) winds and (b) temperature during April 2008.

Figure 4 shows the average CO concentration and CO spread for the month of June 2008 after the 2 month spin-up. Here we highlight the utility of the current setup (online CTM) to generate physically and dynamically consistent spread in CO based on systematic propagation of errors in meteorology (transport term in CO continuity equation) and assumed errors in CO emissions. CO spread varies across the emission and transport regions of CO. The highest spread can be seen in the main source regions (i.e., mostly over populated areas like China and biomass burning areas like Equatorial Africa). Lower CO spread can be seen in the Southern Hemisphere mainly due to lower emissions (less land/biogenic and anthropogenic presence). Conversely, we see higher spread in the tropics and Northern Hemisphere mostly due to higher emissions. Finally, the influence of transport in the CO spread can be easily seen over the Pacific.

### 3.1.2. IASI, MOPITT, and Combined Runs

We carried out three additional sets of assimilation experiments including jointly assimilating conventional meteorological

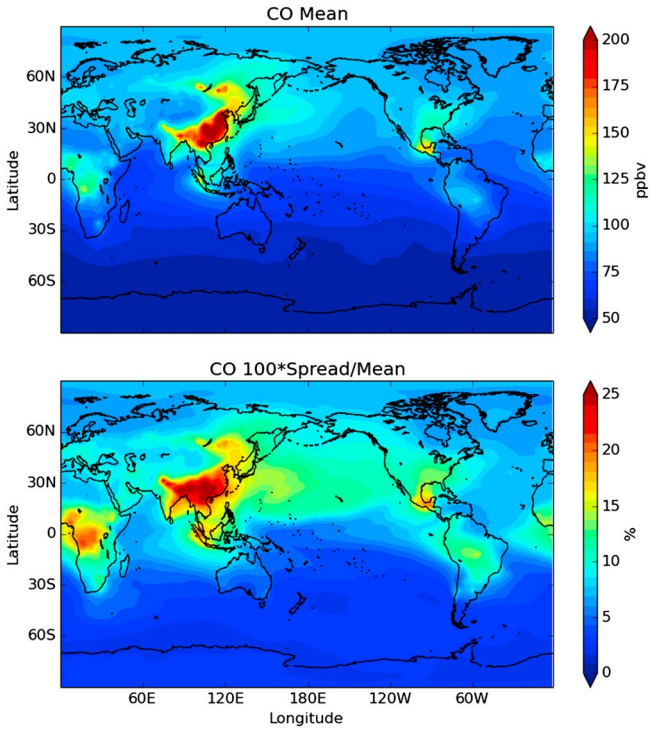


**Figure 4.** Average tropospheric (surface, 200 hPa) (top) CO field and (bottom) relative CO spread in percent, for June 2008 determined from the control run.

observations with (1) MOPITT CO (MOPITT assimilation run (MR)), (2) IASI CO (IASI assimilation run (IR)), and (3) MOPITT and IASI CO (Double assimilation run (DR)), see Table 2. These experiments are conducted for June and July 2008. We use the ensemble CO at the end of the spin-up (31 May) as initial conditions for these experiments. We consider June 2008 as a spin-up period during which the data assimilation system itself is evaluated, and July 2008 as well-constrained CO fields where the assimilation impacts of each instrument are diagnosed.

Figure 5 shows the time series of OmF, OmA, and RCRV for MR and IR. Here we consider several retrieval cases: (1) all observations (Figures 5a and 5b), (2) observations with low sensitivity to the lowermost troposphere (LMT) peaking above 700h Pa (Figures 5c and 5d), and (3) observations with high sensitivity to the LMT peaking below 700 hPa (Figures 5e and 5f). Based on Figure 2 and discussion on retrieval sensitivity, observations for Case 2 are most likely representative of CO over remote regions (transported and free tropospheric CO) but excluding IASI observations that are sensitive over remote regions. Observations for Case 3 can be thought of as CO over source regions (near surface CO over land close to emissions). For all cases, (Case 1), the global statistics of OmA in MR and IR is always lower than the OmF showing that CO data assimilation is generally effective in bringing the modeled CO closer to either MOPITT or IASI. However, the RCRV score for Case 1 indicates values under 1.0 for both MR and IR (around 0.6 and 0.8, respectively) suggesting that globally the error estimates are larger than the actual distance between model CO forecast and observations. This sign of "overfitting" is more evident in MR. We elucidate the cause of this overfitting by comparing the statistics for Case 2 and Case 3 relative to Case 1. The RCRV score for Case 2 is significantly lower than 1.0 especially in MR, while it is close to 1.0 for Case 3 for both MR and IR. This suggests that the global statistics are driven by retrievals sampling and values of CO. Statistics of OmF are expected to be low as magnitudes of free tropospheric CO are about a factor of 2 lower than CO near source regions and errors in model transport are relatively lower than emissions. In the beginning of the assimilation, lower RCRV and lower OmF statistics can be found in Case 2 than Case 3 of MR and IR. This consequently drops and stabilizes after about a week of assimilation similar to Case 1. We also note here that constraining surface CO in the model through assimilation of higher LMT sensitive retrievals (Case 3) near source regions aids in bringing modeled free tropospheric CO closer to observations provided transport and CO sink are captured well in the model. This is true with MR, which exhibits larger OmF statistics than IR due to higher LMT sensitivity in MOPITT combined with large underestimation of anthropogenic emissions in CAM-chem [e.g., *Shindell et al.*, 2006] and the use of monthly mean wildfire emissions. This sign of overfitting is exacerbated by larger retrieval error estimates (e.g., superobservations and retrieval prior error) and our assumption of uncorrelated errors in retrieved CO profiles. However, a simple tuning of observation error may be prone to assimilating instrument/retrieval noise instead. Further evaluation of the assimilation performance through comparison with independent measurements is described and discussed in section 4 of this paper. Briefly, our comparisons show improvements in statistics across all regions in both MR and IR.

### 3.2. Comparison of DA Increments (AmF) Runs

In this section, we investigate the average adjustments of model CO fields in the assimilation for MR and IR as well as DR. Figure 6 displays the root-mean-square (RMS) of the relative increments (AmF/F) defined here as

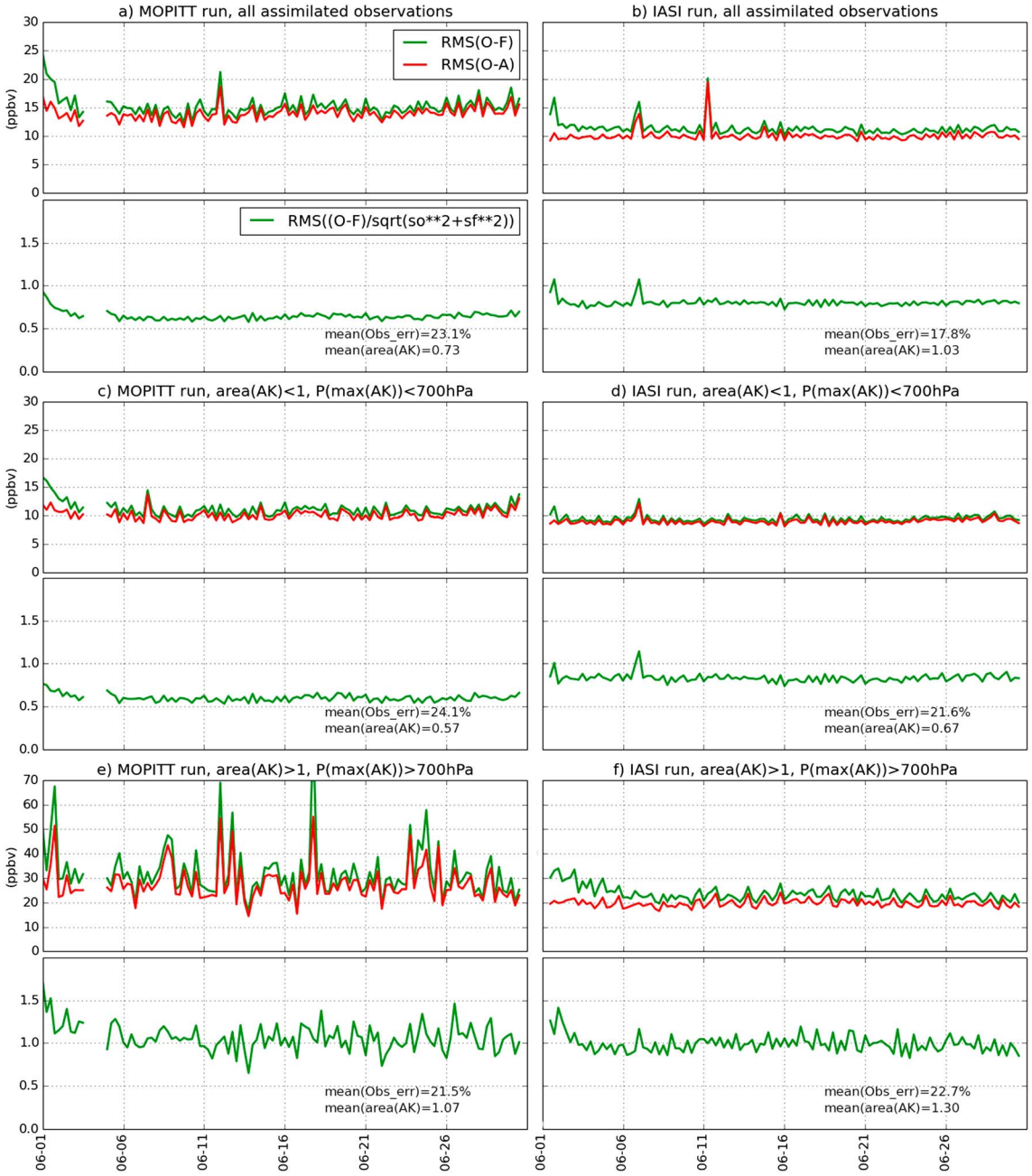


**Figure 5.** RMS of observation minus forecast (OmF, green lines top plots) and observation minus analysis (OmA, red lines top plots) and RMS of RCRV (green lines bottom plots) for: all (a) MOPITT and (b) IASI observations, (c and d) observations remote from sources, and (e and f) observations close to sources during June 2008.

posterior ensemble mean (analysis) minus prior ensemble mean (forecast) divided by the prior mean. We use the RMS of these increments relative to the forecast as a metric to identify short-term systematic error patterns in the model. Here we choose the RMS statistic rather than the mean as it represents the overall variability of the increments expressed in terms of precision (standard deviation) and bias.

Overall, the RMS on the relative increments in IR are higher than in MR. This can be mainly attributed to the combined effect of the more frequent sampling (broader spatiotemporal coverage), important free tropospheric sensitivity and lower relative retrieval errors in IASI. This is evident in the middle to upper troposphere where large increments persist across the transport pathways of CO (e.g., Asian CO advected across the Pacific toward North America). As described earlier, the averaging kernels in IASI retrievals suggest sensitivity

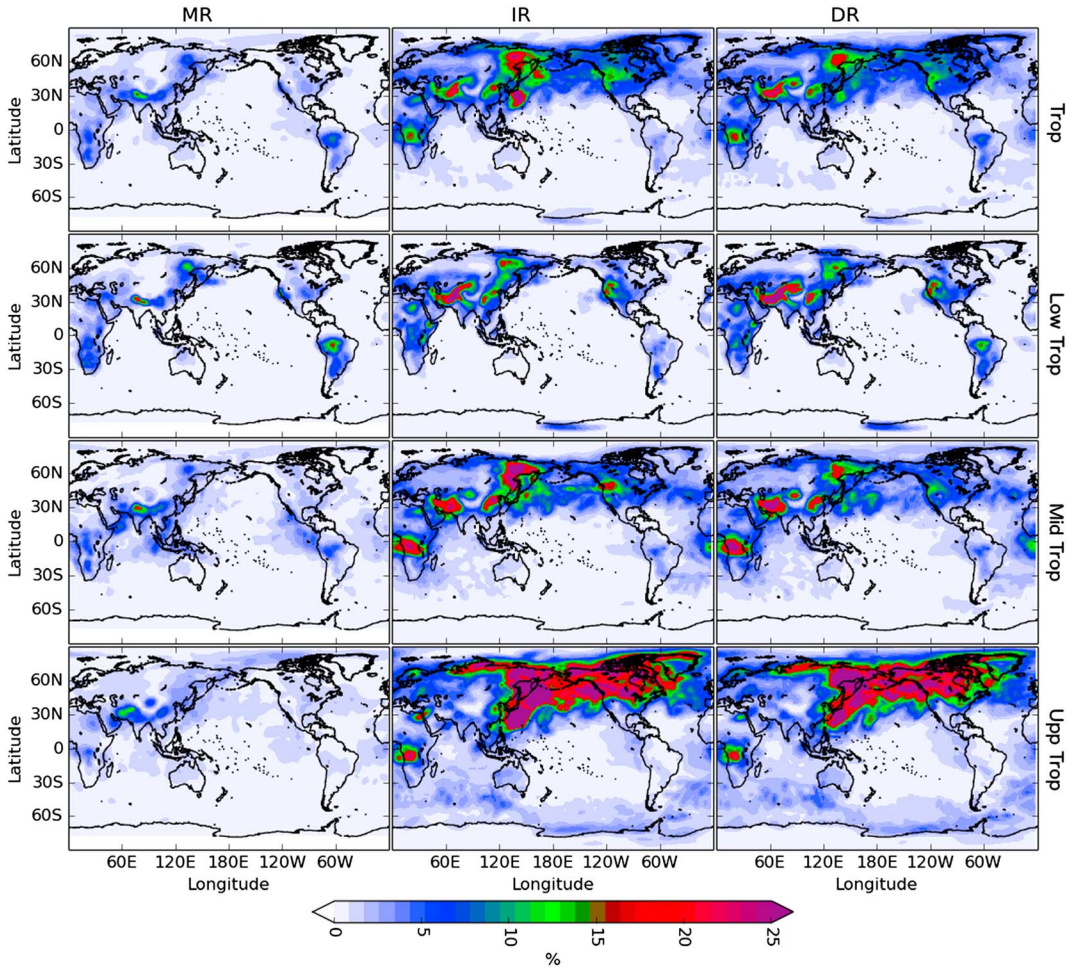


**Figure 6.** RMS of relative increments (posterior state minus prior state divided by the prior state) during July 2008 for (first column) MOPITT assimilation (MR), (second column) IASI assimilation (IR), and (third) MOPITT + IASI assimilation (DR). Different layers of the troposphere are diagnosed: full troposphere (Trop, surface, 200 hPa), lower troposphere (Low Trop, surface, 800 hPa), middle troposphere (Mid Trop, 800 hPa–400 hPa), and upper troposphere (Upp Trop, 400 hPa–200 hPa).

to the troposphere regardless of geographical region and atmospheric conditions. IR also shows large increments over the source regions (lower troposphere) but with patterns extending around emission locations relative to MR, which is consistent with its coverage and sensitivity. On the other hand, MR shows more localized (in both horizontal and vertical) increments over the source regions. There are obvious MR increments in the Amazon, South Africa, and northern India that differ with IR. While over the Amazon neither IR nor MR show upper tropospheric increments, MR shows significant lower tropospheric increments. The South Africa increments are most likely signatures of convective lifting, while the Amazon increments are most likely related to MR sensitivity emissions. These are either convective regions or large CO sources for which MOPITT has relatively larger constraints (high LMT sensitivity over land/daytime and reasonable sensitivity in the upper troposphere). However, MOPITT TIR/NIR retrievals are dependent on atmospheric and surface parameters that considerably decrease the sensitivity over the oceans and over unfavorable land conditions (e.g., night, low thermal contrast, surface emissivity, and among others).

The third column of Figure 6 shows the RMS of relative increments in DR. In general, the DR increments are combinations of MR and IR increments indicating complementary information between IASI and MOPITT under certain conditions. Consistent with previous discussion (IR versus MR), MOPITT detects a biomass burning signature in the lower troposphere of the Amazon basin that is not that well detected by IASI. Such strong CO signatures that are close to the surface can be constrained by MOPITT. IASI detects CO not directly at the surface but above, where the CO source signature is weaker, and hence, IR provides smaller increments. On

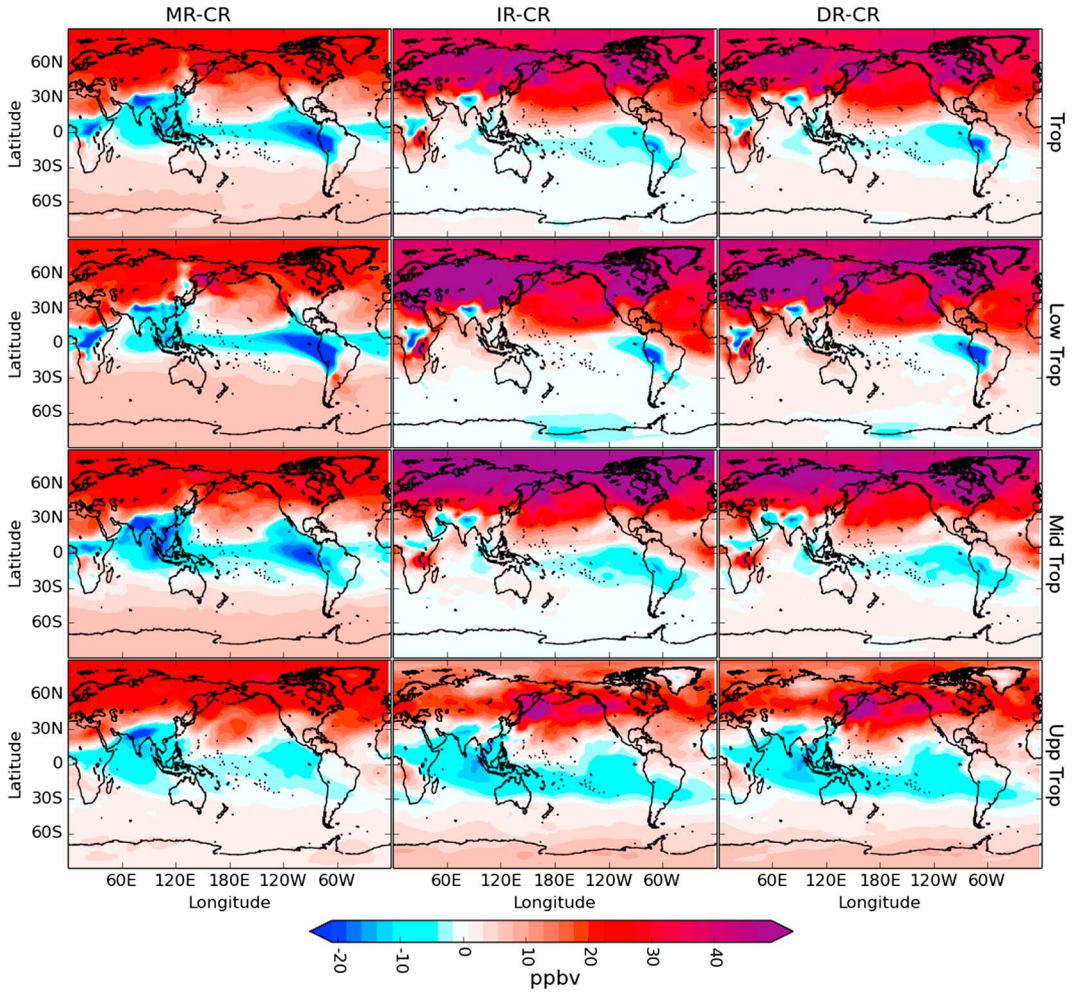


**Figure 7.** Differences between assimilated CO and CO from control run during July 2008: (first column) MOPITT assimilation minus control (MR-CR), (second column) IASI assimilation minus control (IR-CR), and (third column) MOPITT + IASI assimilation minus control (DR-CR). Different layers of the troposphere are diagnosed: full troposphere (Trop, surface, 200 hPa), lower troposphere (Low Trop, Surface, 800 hPa), middle troposphere (Mid Trop, 800 hPa–400 hPa), and upper troposphere (Upp Trop, 400 hPa–200 hPa).

the other hand, above the northern Pacific in the middle to upper troposphere, DR increments are smaller than IR increments suggesting the impact of MOPITT in providing constraints on the sources (here Asia) that are long-range transported over Pacific, resulting to lesser DR increments in the remote regions from the sources. In summary, the multispectral retrievals of MOPITT provide additional sensitivity toward the surface that improved constrains on CO over source regions, while the daily global coverage and broader sensitivity of IASI for the entire troposphere provides best constraints downwind of the sources.

### 3.3. Comparison of Assimilated CO Fields Runs

We present in Figure 7 the mean differences between the assimilation experiments (MR, IR, and DR) and the control experiment (columns) for several regions of the troposphere (rows). This is to diagnose whether the assimilated CO fields are on average increased, decreased, or unchanged by assimilating MOPITT and/or IASI. We find a consistent and significant increase in CO for all experiments across the Northern Hemisphere. This increase is larger with IR (up to 50 ppbv) than MR (up to 30 ppbv). As discussed in previous section, MR mostly provides constraints near source locations whereas IR increments are broader (globally and across the troposphere). The large underestimation of CO in NH [e.g., *Lamarque et al.*, 2012; *Tilmes et al.*, 2015] has been corrected in all assimilation runs. This bias is likely due to an underestimation of CO and VOC emissions from anthropogenic and biomass burning inventories as previously pointed out by *Stein et al.* [2014], *Emmons*

*et al.* [2015], *Tilmes et al.* [2015], and *Monks et al.* [2015]. However, it is difficult to fully ascertain the relative contribution of the uncertainties in emission and chemical loss due to OH from this analysis alone.

We also find that in the tropics MR shows larger decreases in the CO fields relative to IR. This is the case in the lower to middle troposphere over sources regions in Equatorial Africa, Amazonia, and northern India (about 10–20 ppbv). The pattern of decrease is also spatially broader (in horizontal and vertical) for MR than IR. Since the MR increments described earlier are localized near the sources, this suggests the propagation of the model adjustments near the source toward the outflow regions. On the other hand, the IR increments are broader resulting in lower decreases in CO fields downwind (more corrections in the transport pathway). In any case, both MR and IR suggest a decrease in CO fields in the tropics throughout the troposphere. It is interesting to note that *Jiang et al.* [2013] showed that assimilating MOPITT V5J surface level retrievals results in decreases in direct CO emissions in tropical convective regions and a strong decrease of middle and upper tropospheric CO, which is consistent with our results.

In the case of DR, the differences are very similar to IR indicating the dominant impact of assimilating IASI in CAM-chem. This is true in the NH with patterns of increase in CO as well as in the tropics with a tendency to lowering CO. We find that assimilating IASI has the ability to correct errors in model transport due to its broader coverage and sensitivity and lower errors.

### 3.4. Synergies Between MOPITT and IASI

A common definition of synergy is the creation of a whole that is greater than the simple sum of its parts. Here we design the following synergy diagnostic, which is based on equation (4) of *Barré et al.* [2014], to diagnose whether combining MOPITT and IASI retrievals can bring any added value:

$$\mathrm{SYN} = [|\mathrm{DR\text{-}CR}|\text{-}|\mathrm{IR\text{-}CR} + \mathrm{MR\text{-}CR}|]/\mathrm{CR}. \tag{14}$$

This diagnostic, which can be negative, zero or positive, is the difference between the magnitude of the impact of DR (i.e., $|\mathrm{DR} - \mathrm{CR}|$) to the magnitude of the sum of the impacts of IASI-only and MOPITT-only assimilation (i.e., $|\mathrm{IR} - \mathrm{CR} + \mathrm{MR} - \mathrm{CR}|$) relative to CR. It can be interpreted as follows:

1. A negative synergy means that the DR effect is lower than the sum of IR and MR effects. This can be interpreted as redundant information that the two assimilations bring in the analysis. For example, IASI assimilation already corrects the fields and MOPITT has less or nothing to correct afterwards.
2. A zero synergy means the DR effect is exactly the sum of IR and MR effects. In this case the two retrievals assimilated are complementary and the information they bring into the system is not redundant.
3. A positive synergy means that the DR effects are more than the sum of IR and MR effects. This is considered as the actual synergy following the definition given above. As an example, consider the first retrieval assimilated corrects the CO field. The second retrieval samples the same field and when assimilated further corrects the CO field. This synergy can be effective in the case of large forecast errors that cannot be constrained by one type of retrieval alone.

It should be noted that synergies can also be affected by the nonlinearity of the chemical model; e.g., CO changes by data assimilation can feedback on the CO production and loss through changes in OH. For example, local large increase in CO potentially decreases local OH abundance (CO loss). This change could result to decrease in the oxidation of VOCs (CO production). In this study, however, we find very few instances of significantly large CO changes that lead to strong local chemical response in the model. This is due to the large spatial scale (2°) of our modeling system. Hence, we find that the CO impact on the model is mainly driven by frequent revisit time (1 to 3 days) of MOPITT and IASI (assimilation effect) compared to model chemical response.

Figure 8 presents synergy diagnostics as a monthly average (Figure 8, left) and instantaneous field at 15 July 2008 00UTC (Figure 8, right) for different regions in the troposphere (rows). On average, the synergy is negative with the strongest negative values over NH high latitudes. This can be attributed to the longer CO lifetime in this region, where the dynamics of the system are driving its distribution and abundance, and hence resulting in less observational frequency necessary to constrain the field. The CO lifetime is longer in higher latitudes due to its dependence on OH distribution, which decreases from the tropics to the poles [*Monks et al.*, 2015, *Emmons et al.*, 2015]. As such, the two types of constraints from MOPITT and IASI are most likely redundant in this region. In the tropics, however, we see close to zero synergy values indicating the complementary

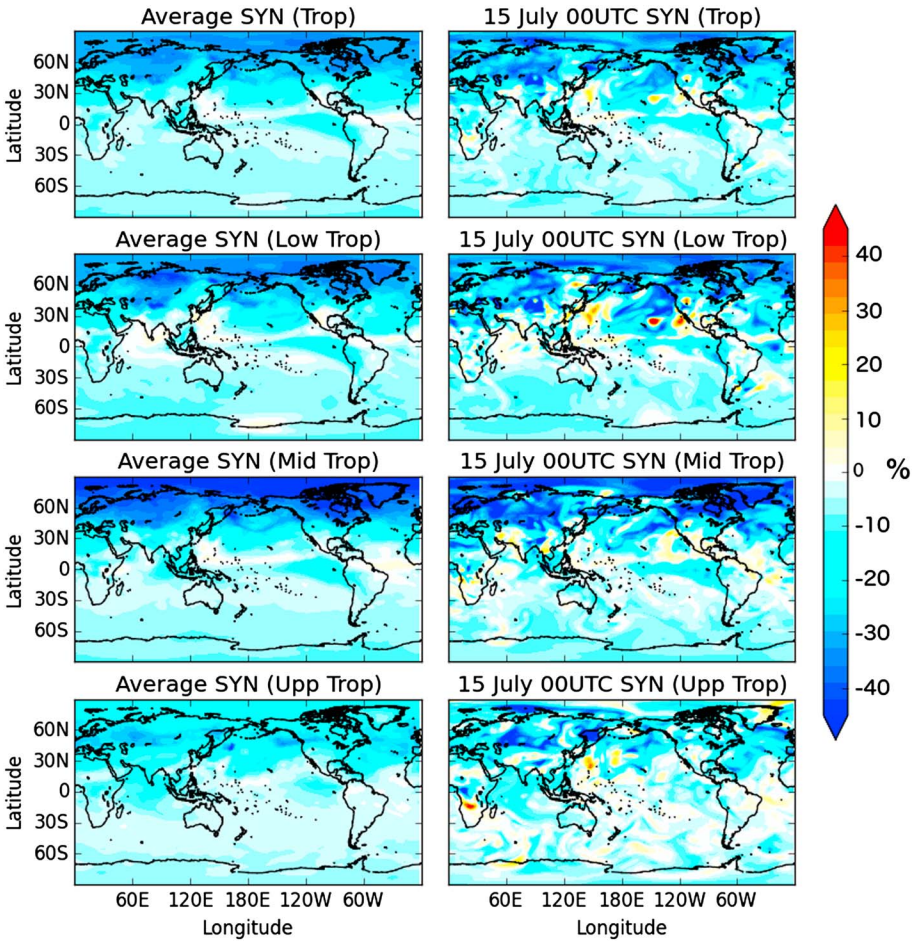


**Figure 8.** Values of the synergy relative to the control run. The left column is the July 2008 average while the right column is the 15 July 2008 00:00 UTC statistics. Different layers of the troposphere are diagnosed: full troposphere (Trop, surface, 200 hPa), lower troposphere (Low Trop, surface, 800 hPa), middle troposphere (Mid Trop, 800 hPa–400 hPa), and upper troposphere (Upp Trop, 400 hPa, 200 hPa).

information of MOPITT and IASI especially near source and outflow regions. For the instantaneous synergy fields, we find similar patterns but with larger spatial variations. Over regions where forecast errors remain large (e.g., biomass burning and urban regions), the combined assimilation of MOPITT and IASI can be synergistic. Positive synergies can be seen in either the source region (southern Africa) or CO plumes transported downwind (over Pacific Ocean).

## 4. Data Assimilation System Evaluation

In this section, we evaluate the assimilated CO fields (MR, IR, and DR) against independent measurements and retrievals to provide a measure of DA system performance. We grouped our evaluation based on the specific domains of available observations (i.e., global/ Thermal Emission Spectrometer (TES), Arctic/Polar Study using Aircraft, Remote Sensing, Surface Measurements and Models, of Climate, Chemistry, Aerosols, and Transport (POLARCAT), and Continental United States/U.S. Environmental Protection Agency (EPA)).

### 4.1. Global Evaluation Against TES

Tropospheric Emission Spectrometer (TES) [*Beer et al.*, 2001; *Beer*, 2006; *Rinsland et al.*, 2006] is an infrared Fourier transform spectrometer onboard the Aura satellite. Similar to MOPITT and IASI, TES measures TIR radiances in the CO band. TES nadir footprints of $5 \times 8$ km are separated by around 60 km along the orbit track. TES retrievals of CO profiles are described by *Bowman et al.* [2006] and validated by *Luo et al.* [2007a] using aircraft measurements. We use the TES measurement to evaluate the data assimilation

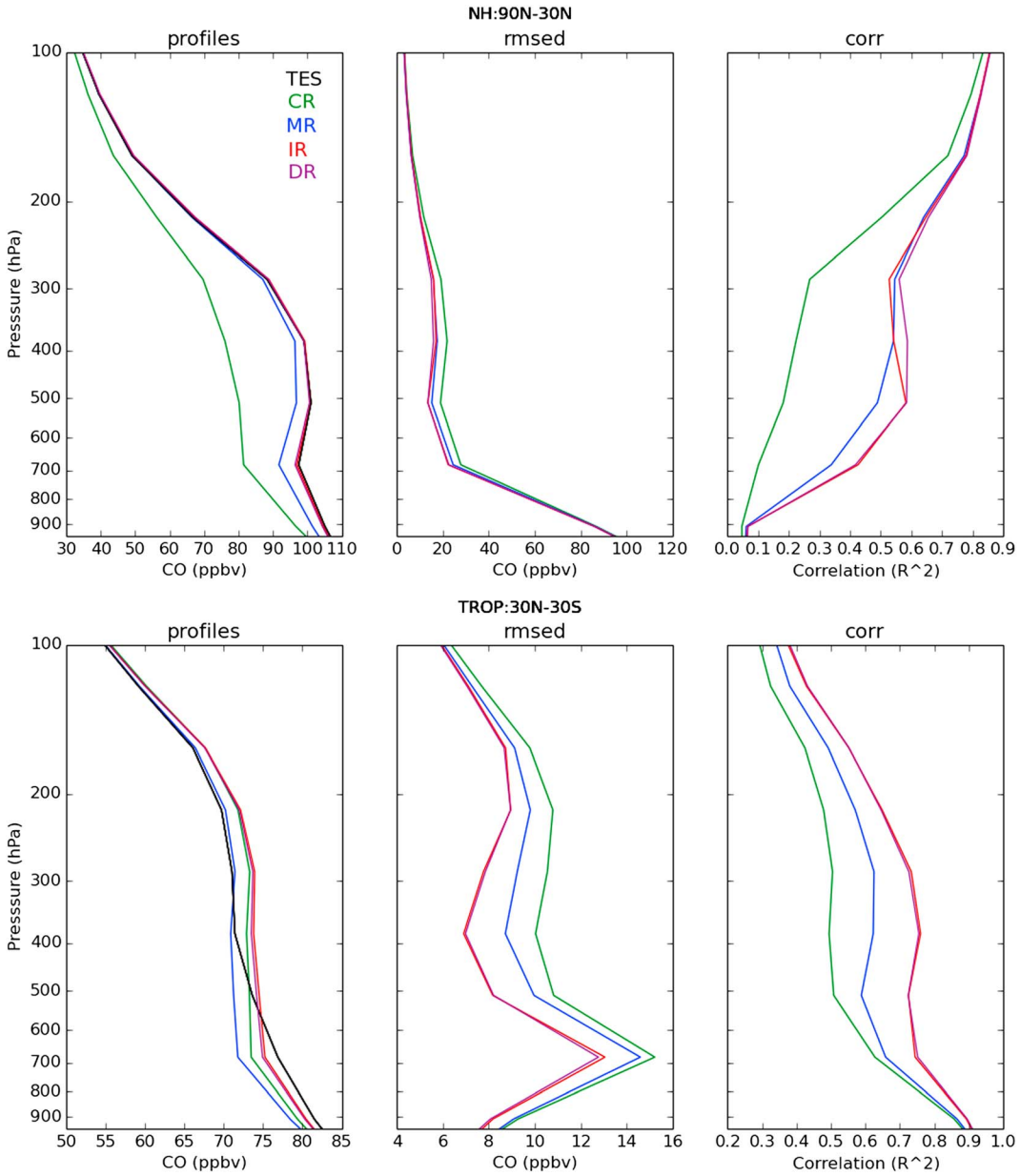


**Figure 9.** Comparison between CO from DA experiments and TES CO during July 2008. First column is the comparison of average profiles, second column is the unbiased root mean square error of the assimilation run to the TES profiles, and third column is the correlation between TES profiles and assimilation runs. First row: Northern Hemisphere (NH), second row: tropics (Trop).

performance on the free troposphere at global scale. To evaluate the model against TES retrievals, we smoothed the model experiments with the associated TES CO averaging kernel matrix and retrieval and a priori profiles using equation (8.1). Similar to IASI, TES CO averaging kernels mostly peak in the free troposphere and tend to be close to zero toward the surface. An example of TES CO averaging kernels can be found in Figures 10 and 11 of *Luo et al.* [2007b]. The average retrieval relative error ranges from 10% to 20% for TES CO profile. It is important to note that TES sensitivities peaks on free tropospheric levels. TES averaging kernels exhibit similar shapes as IASI and MOPITT over remote regions. Over source regions, the MOPITT averaging kernels peak at the surface which can result to data assimilation increments near the surface contributing to the free tropospheric constraint through transport of CO (see section 3.3).

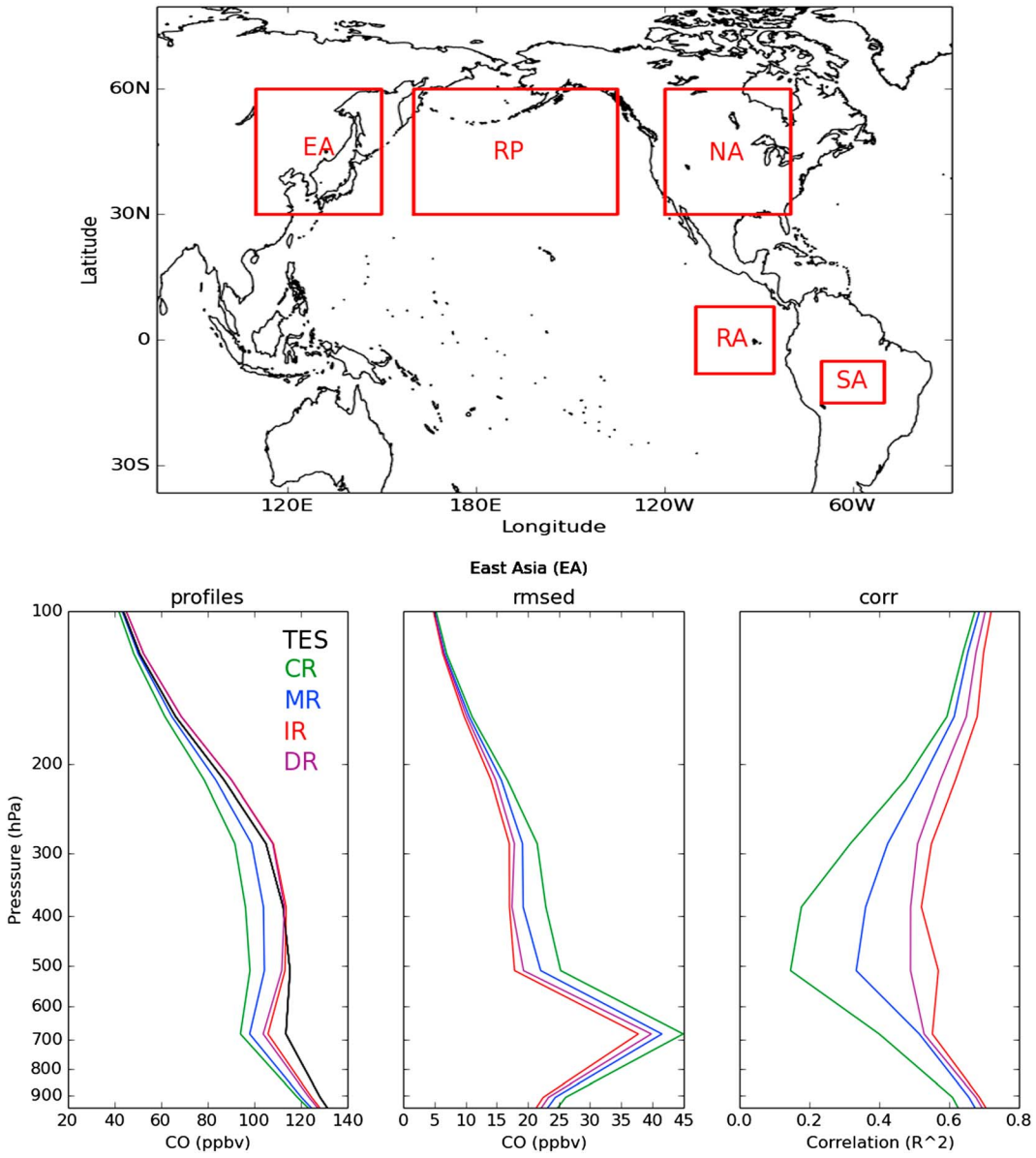


**Figure 10.** Same TES evaluations as in Figure 9 but for the specific regions shown in the top plot.

Figure 9 displays the overall statistics of the different assimilated CO (MR, IR, and DR) and modeled CO (CR) relative to TES CO across broad regions of the globe. This includes the mean profiles unbiased root-mean-square error (RMSE) (RMSED), and correlation coefficients across the month of July 2008 in the Northern Hemisphere and Tropics. Over the Northern Hemisphere, the statistics show that CR is negatively biased up to 25 ppbv in the free troposphere relative to TES. This bias is reduced to less than 5 ppbv for MR and to almost no bias for IR and DR. The RMSED is slightly reduced for all assimilation experiments, while the correlation is strongly improved in the free troposphere, especially with IR and DR. Over the tropics, CR CO exhibits low systematic mean error (under 5 ppbv), a slight negative bias in the free troposphere and a slight positive bias in the upper troposphere, relative to TES CO. MR reinforces the negative bias in the middle troposphere and corrects the positive bias in the upper troposphere. IR and DR slightly correct the negative bias in the middle troposphere. They also show best improvements in RMSED and correlation with MR showing modest results. Over the Southern Hemisphere, the bias in CR CO relative to TES is small with a 5 ppbv overestimation in the middle troposphere (not shown). While the low bias over the tropics is

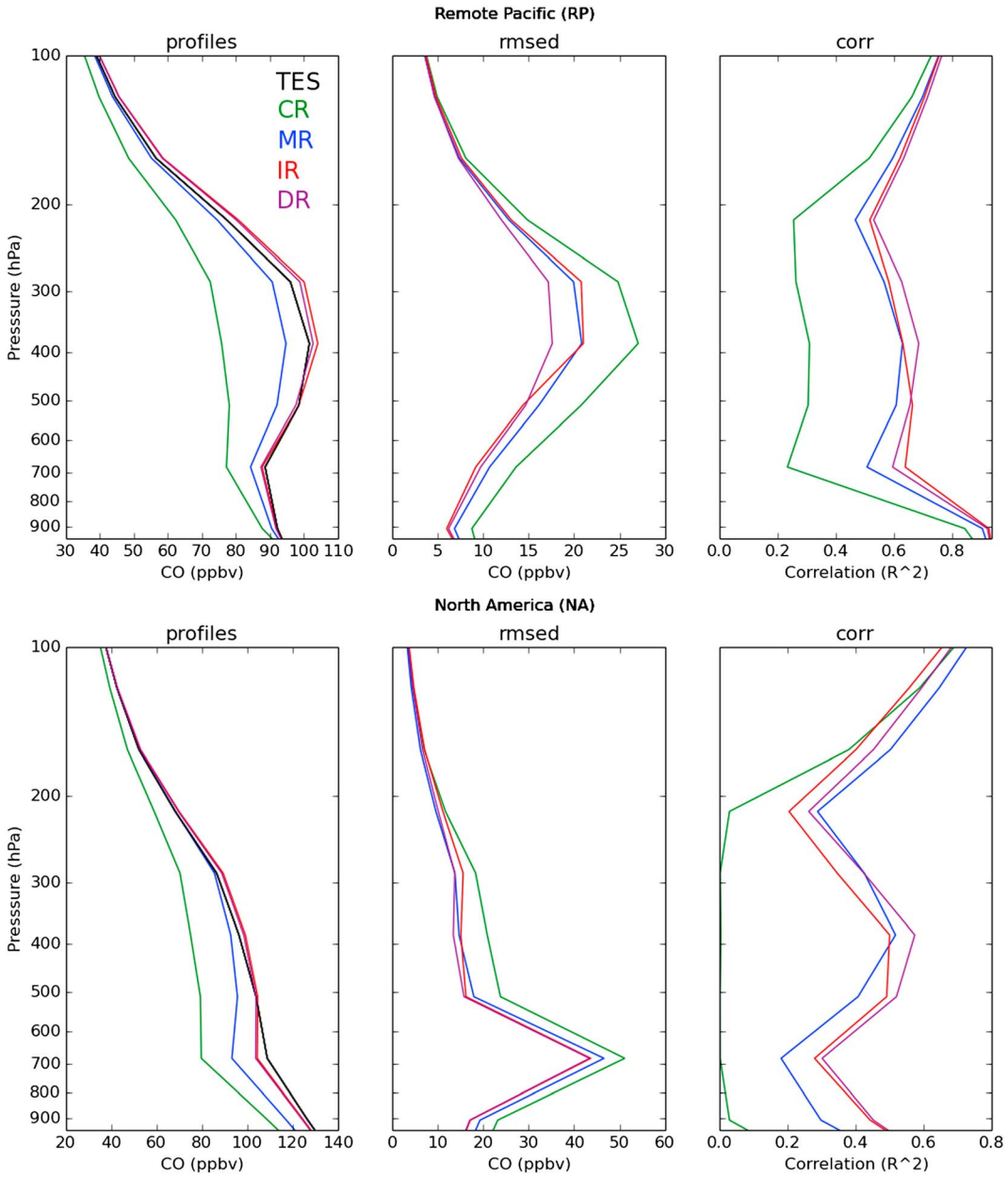


**Figure 11.** Same TES evaluations as in Figure 9 but for the specific regions shown in the top plot of Figure 10.

not improved in the data experiments, IR and DR experiments slightly improve the RMSED and correlation consistent with the "information content" of IASI.

Figures 10–12 present similar statistics of system performance relative to TES, but now focusing on specific regions of the globe. The selected regions include EA (East Asia), RP (Remote Pacific), NA (North America), RA (Remote Amazonia), and SA (Southern Amazonia). We selected EA, RP, and NA (Figures 10 and 11) to diagnose the impact of assimilating CO retrievals across the northern extratropics on constraining continental CO and long-range transport over the Pacific Ocean. EA includes key anthropogenic sources (i.e., northern China, Korea, and Japan) and biomass burning source from Siberia during July 2008. The IR and DR experiments perform better than MR owing to IASI's coverage. This is particularly the case during summer over East Asia, where very cloudy conditions limit the number of valid retrieved pixel [*Barré et al.*, 2015]. A broader coverage, like IASI, provides more opportunity to sample cloud free scenes in this region. Over RP where Asian pollution is typically transported, all DA experiments present almost the same performance on correlation

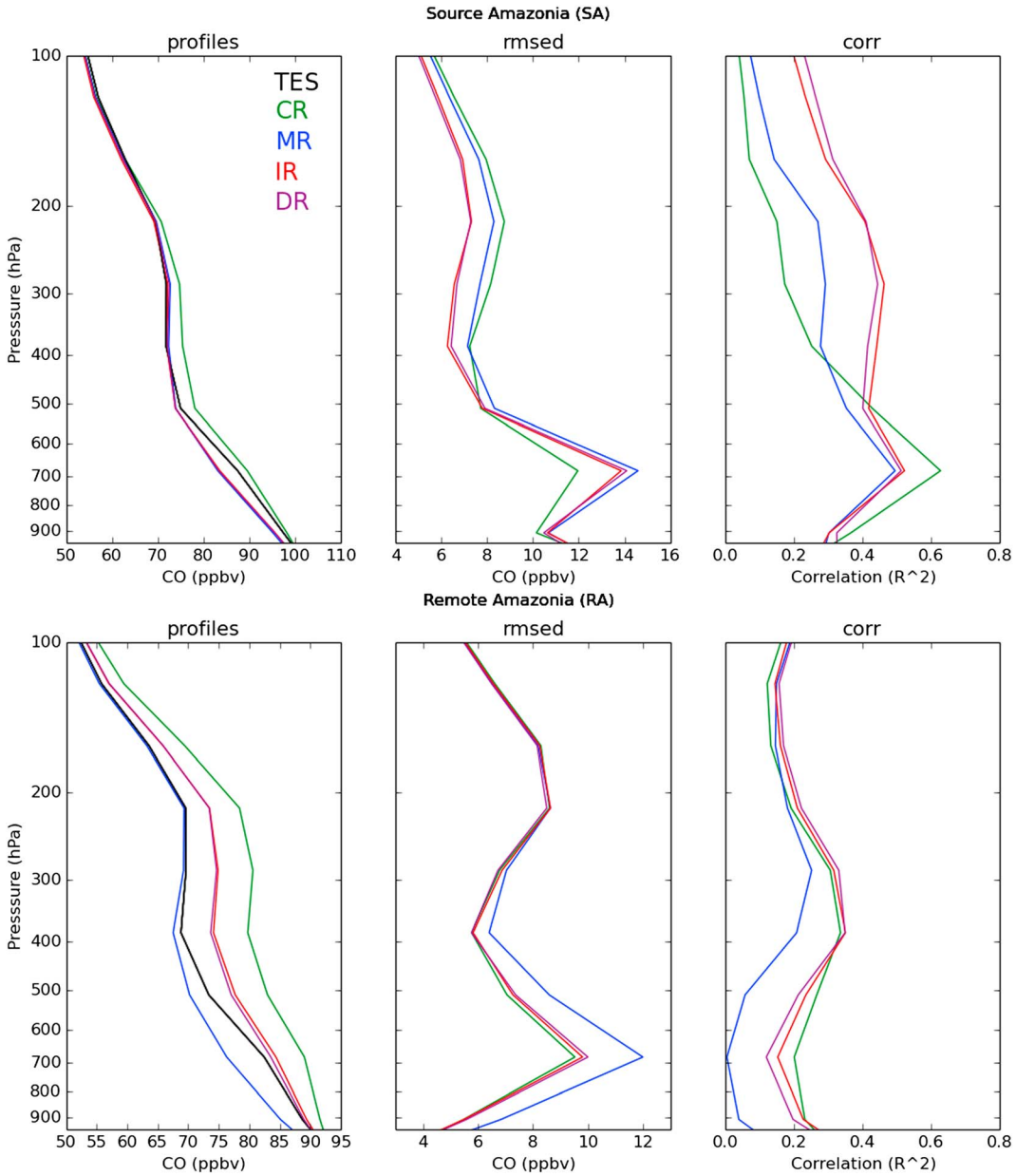


**Figure 12.** Same TES evaluations as in Figure 9 but for the specific regions shown in the top plot of Figure 10.

and RMSED. MR on the other hand shows smaller bias correction. Constraining CO close to the sources (MOPITT) or globally in the free troposphere (IASI) provides very similar forecast statistic scores in this region. Slight synergistic effects can be observed on the middle troposphere as CO in DR is closer to TES CO in terms of bias, RMSED, and correlation than CO in IR and MR. Similar statistics can be seen in NA for MR, IR, and DR.

As discussed earlier (section 3.3), MR generates stronger and more extended patterns of decreasing CO relative to IR and DR over the tropics (Figure 7). We selected SA and RA to elucidate this difference (Figure 12). Over the source region (SA), all DA runs degraded the forecasts in the lower and middle troposphere (from surface to 600 hPa on TES vertical levels), whereas the runs improved forecasts in the upper troposphere relative to TES CO. The degradation is interpreted to be mainly due to errors in modeled vertical transport rather than bias in IASI and MOPITT retrievals given similar DA impact on MR and IR. This is supported by findings of *Jiang et al.* [2013] among others that CTMs struggle to represent vertical transport of fire emissions in the tropical region. Over RA, only MR significantly degraded the forecasts, mostly reversing the CO bias from positive (CR) to negative

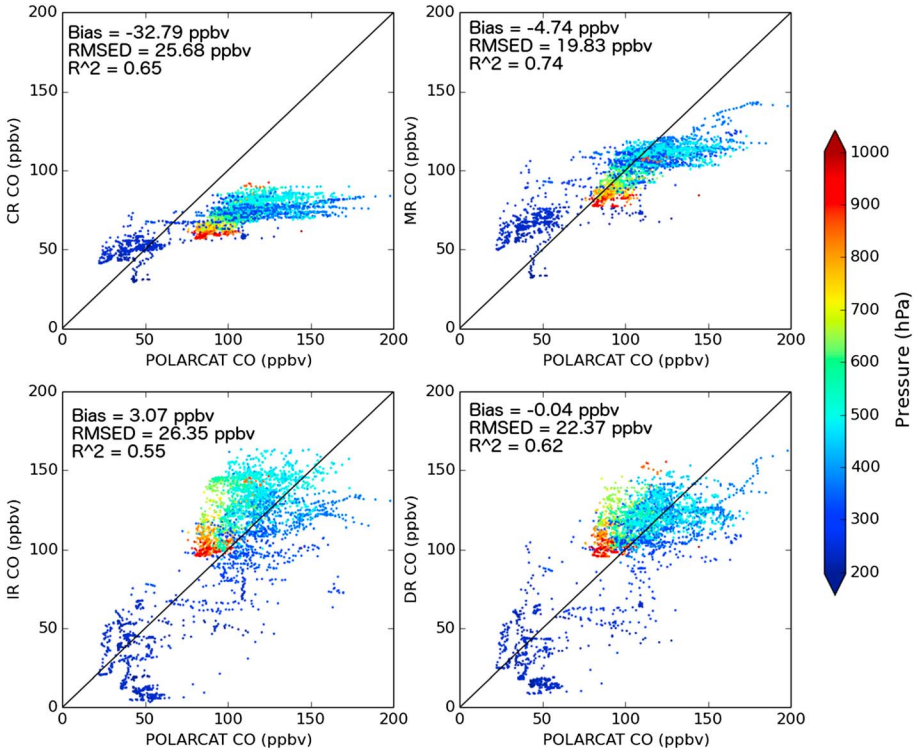


**Figure 13.** Evaluation of assimilation runs against POLARCAT flights from 30 June 2008 to 14 July 2008. CR, MR, IR, and DR cases are shown in the top left, top right, bottom left, and bottom right, respectively. Each plot provides corresponding statistics: Bias, unbiased root mean square error (RMSED) and correlation.

and increasing (decreasing) the RMSED (correlation) in the middle and lower troposphere. IR and DR only improve the bias relative to TES CO. These results suggest that neither IASI nor MOPITT assimilation is performing well in this region. Currently, this issue is not fully understood. The current results suggest that constraints close to the CO sources (MR) over the tropics generate additional error due to vertical transport errors, transporting strong data assimilation increments at wrong atmospheric levels. This error is propagated and remains in the model toward the remote regions. If the constraint is over tropical remote regions (IR and DR) then the transported error is partially corrected. Because IASI sensitivity is strong over remote areas below 400 hPa, this error is transported and corrected over remote areas and in the upper troposphere. Conversely, because MOPITT sensitivity is weak over remote areas and below 400 hPa, this error is transported and not corrected over remote areas and in the middle and lower troposphere. Examination of Figure 2 show that MOPITT sensitivity is comparable to IASI sensitivity in the upper troposphere although significantly lower in the middle and lower troposphere over remote regions. This is reflected in Figure 12 where MR removes the bias relative to TES in the upper troposphere and significantly degrades the scores in the middle and lower troposphere while a residual bias is still observed in IR and DR from the lower troposphere to the upper troposphere.

### 4.2. Arctic Evaluation Against POLARCAT

The POLARCAT (Polar Study using Aircraft, Remote Sensing, Surface Measurements and Models, of Climate, Chemistry, Aerosols, and Transport) mission is an international project that involved various aircraft platforms (NOAA WP-3D, NASA DC-8, CNRS ATR-42, DLR Falcon-20, and Antonov-30). It was designed to study the impact of pollution on atmospheric composition and climate change in the Arctic. The measurements used in this paper for comparison with our experiments were carried out during the summer campaign (i.e., 30 June to 14 July 2008) to sample Arctic air masses originating from regions influenced by North American, Asian, European, and Siberian emissions. The location of the measurement flights used in this study can be found in Figure 15 of *Emmons et al.* [2015] (from 50°N to 90°N and from 0°W to 160°W). Figure 13 presents scatterplots comparing CO from all experiments with POLARCAT CO. Statistics of the comparisons are summarized in Figure 13. As discussed in the TES comparison, CR is negatively biased (in this

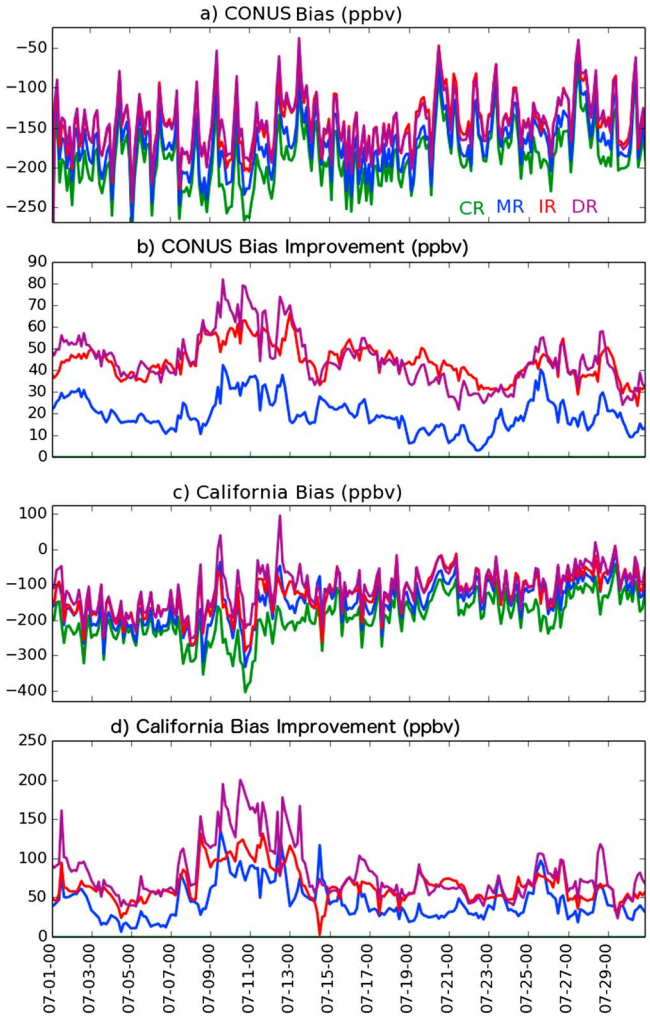


**Figure 14.** Evaluation of control run (CR, green), MOPITT run (MR, blue), IASI run (IR, red), and MOPITT + IASI run (DR, purple) against CONUS U.S. EPA ground rural and suburban stations. (a and c) Time series of each assimilation run for CONUS and California, respectively. (b and d) The corresponding bias improvement relative to CR. *X* axis dates are formatted as month-day-hour.

case by 32 ppbv). Assimilation reduces this bias to −4 ppbv for MR, to +3 ppbv for IR and to almost no bias for DR. In terms of RMSED and correlation, MR shows the best improvement whereas CO in IR was slightly degraded. This can be interpreted by IR significantly adjusting the CO fields remote to the source regions as opposed to MR mostly constraining Arctic CO close to its sources. In the IR case, increments that are not advected during several forecast model cycles can lead to less physical CO variability. Errors in data assimilation increments can be due to errors in IASI measurements generating noise in forecast CO fields or sampling errors in forecast error covariance matrix (calculated from the ensemble statistics) generating spurious correlations during the analysis of the modeled CO field. *Kerzenmacher et al.* [2012] has found that IASI retrieval errors may be underestimated over polar latitudes. In this study, similar error underestimation can lead to larger analysis increments from a number of retrieval noise assimilated in CAM-Chem. This potentially explains the degradation in RMSED and correlation for IR and DR in polar latitudes. Improvements in MR [1]suggest that the CO lifetime in the extra-tropics (more precisely in high latitudes) is well represented in the model and that the bias in CR can be attributed mostly to emissions.

### 4.3. Continental and Regional Evaluation Against U.S. EPA

Here we use the U.S. EPA (Environmental Protection Agency) ground measurement sites over the Continental United States (CONUS). The surface monitoring data used in this study are available for download from the U.S. EPA's Air Quality System database (http://www.epa.gov/ttn/airs/airsaqs/detaildata/downloadaqsdata.htm). Since the spatiotemporal resolution of the forecast is coarse (around 2° in horizontal and 6 h) to represent accurately the CO surface variability over CONUS, we only selected sites with similar coarser representativeness (i.e., sites designated as rural and suburban) and extracted CO data every 6 h over July 2008. The suburban monitoring sites could be often located near strong localized pollution sources creating a strong source-to-receptor relationship that is a challenge to duplicate in coarse model resolution [*Pfister et al.*, 2011]. We hence expect the models and data assimilation experiments to be significantly negatively biased, due to the difference of representativeness between the surface sites (local measurements) and the model having a $2 \times 2°$ representative grid box. We used all regulatory measurements with precision of 0.1 ppmv. Despite this low precision, these surface observations can be used for evaluating the overall performance at the surface. This is the reason why we use only those data to diagnose the surface bias over large areas (CONUS and California). Figure 14 provides time series of average bias for the entire CONUS and for stations located in California, as well as a time series of bias improvements (e.g., $|\text{bias(CR)}| - |\text{bias(MR)}|$) in MR, IR, and DR.

For the entire CONUS, the surface CO bias is improved by 50 ppbv in IR and DR and 25 ppbv for MR. For California sites, IR and MR show similar performance with a bias reduction around 50 ppbv. This suggests the larger impact of coverage (overpass frequency) in constraining surface CO over moderately remote regions (rural) and near to source regions (suburban). While the sensitivity of IASI retrievals does not peak directly at the surface (more at the upper boundary layer levels; Figure 2), it appears to be capable to partially constrain the surface layers (possibly through boundary layer mixing and ventilation). Over California where EPA sites are closer to strong CO sources, the impact of assimilating MOPITT (MR) is enhanced. This is because of very favorable conditions (very few clouds and very good thermal contrast) for MOPITT in combination with its enhanced surface sensitivity.

Complementary effects (where synergy is close to 0) can also be observed in Figure 14. DR CO is most of the time closer to U.S. EPA CO than IR or MR. This is especially the case over California. The bias improvements in DR are higher than in IR and MR. DR provides scores more than twice as good as IR and MR independently (i.e., Figure 14d from 10 July to 15 July), meaning that IASI and MOPITT different capabilities are complementary used in the assimilation process.

## 5. Summary and Conclusions

In this paper, we describe in detail the implementation of the new version of the chemical data assimilation system based on NCAR's CESM-CAM-chem/DART. In particular, we apply the chemical data assimilation system to investigate and assess the impact of assimilating CO retrieved profiles from two instruments (IASI and MOPITT) on constraining the forecast and analysis of CO in CAM-chem. Our working hypothesis, based on detailed examination of the differences between the two data sets, is that the two instruments provide different and complementary capabilities in constraining CO. While the multispectral retrievals from MOPITT have enhanced sensitivity toward the surface and across the main CO source regions, its coverage is relatively limited. On the other hand, retrievals from IASI, while less sensitive to the surface, exhibit sensitivity to the free troposphere across the globe and broader horizontal coverage.

We carried out three sets of experiments to elucidate the nature of the individual (MR and IR) and combined (DR) impacts of these retrievals relative to a control run (CR) and to independent CO measurements corresponding to different spatiotemporal scales (TES, POLARCAT, and U.S. EPA). The overall evaluation against independent data shows that the chemical data assimilation system performs well in terms of bringing significant improvements on the CO forecasts in CAM-chem for all experiments. We also looked closely at key model space diagnostics (DA increments) and differences of assimilated CO fields (MR, IR, and DR relative to CR). We find that MR mostly constrains the CO fields close to the main anthropogenic and biomass burning sources, while IR constrains mostly CO downwind from the source regions. This is generally consistent with our working hypothesis.

This work represents our first step toward assimilating multispecies and/or multiplatform retrieval products into CESM-CAM-chem/DART. Below, we summarize the key insights we found in this work, which may be useful for future chemical DA activities:

1. The coverage of IASI versus the sensitivity of MOPITT plays a large role in the nature of the impacts and constraints. The larger coverage of IASI allows better detection of pollution scenes and transported plumes of high CO concentration. The MOPITT multispectral retrieval provides enhanced sensitivity at the surface over main CO source regions but has weak sensitivity to the middle troposphere over remote regions. Conversely, IASI does not generally have the strong sensitivity at the surface but exhibits sensitivity over the free troposphere. These differences in the two instruments are clearly reflected in the DA increments where the CO fields are constrained according to the instruments' coverage and retrieval sensitivities. The MOPITT increments are mostly in the lower troposphere and close to the major CO sources, while IASI increments are spread more globally and extend throughout the troposphere. Our evaluation with independent measurements indicates that MR does not correct the bias over the Northern Hemisphere as well as IR. IR also shows better performance over anthropogenic source regions (Eastern Asia and CONUS) than MR. However, MR provides equivalent or better results over the NH remote regions (Northern Pacific and Arctic). This is not the case over the tropical regions where MR further degrades the model forecasts.

2. This work points out possible deficiencies in representing CO in CAM-chem. As pointed out in several sections of this paper, the model emissions are mostly responsible for the systematic CO negative bias in NH. MR corrects the CO fields mostly close to the source and removes the bias in its majority. Because MOPITT has limited coverage compared to IASI, it is, however, difficult to quantify unequivocally the relative contribution of errors from the sources and sinks of CO to the NH bias. In the tropics, we find that MR degrades CO in remote regions more than IASI, which we attribute to model error propagation. In particular, our analysis suggests the potential role of errors in model vertical transport in bringing modeled CO further from observations. We note that detailed investigation and diagnostics over longer time of integration are needed to elucidate this issue.
3. The combined assimilation of MOPITT and IASI retrievals in CAM-chem (DR) provides synergistic effects. Here we propose a novel diagnostic to show conditions where the two sources of assimilated information are redundant, complementary, or synergistic. On a monthly average time scale, IASI and MOPITT assimilated retrievals share redundant information. It is shown that redundancy is the strongest over Arctic regions, where CO lifetime is expected to be longer than in lower latitudes. Synergistic or complementary effects are observed over shorter time and regional scales close to the source regions. As an example, bias correction of surface CO over California can be improved synergistically over a few days with DR.
4. One limitation of this work remains on neglecting the off-diagonal terms of the retrieval error covariance matrix that are important for inter-comparison studies. Accounting for retrieval error off-diagonal terms in sequential data assimilation require additional algorithm development that would be addressed in further studies.

## Appendix A: Superobservations

Since the horizontal resolution of the CO satellite data retrievals (around 20 km) is much finer than CAM-chem (2.5° × 1.9°), we adopt the superobservation approach to produce more representative data comparable to the coarser model resolution. In addition, it is computationally cheaper to use superobservations in global satellite data assimilation. The approach is to average the observations (including errors and averaging kernels) across each 1.9° latitude × 2.5° longitude bin. We perform the weighted averaging using relative observation errors as the weights. The weighted average is calculated as

$$\overline{y}_o = \sum_{i=0}^{N} (w_i\, y_i) \tag{A1}$$

$$w_i = \frac{\sigma_i^{-2} y_i^2}{\sum_{i=0}^{N} \left(\sigma_i^{-2} y_i^2\right)} \tag{A2}$$

where $\overline{y}_o$ is the superobservation, $y_i$ is original observation value, $\sigma_i^2$ is the error variance, and $w_i$ is the weight. The error average $\sigma_{\overline{y}}$ can be calculated using the variance-covariance matrix **C** of all the observation errors within the given bin as:

$$\sigma_{\overline{y}} = \sum_{i=0}^{N} \sum_{j=0}^{N} \left(w_i w_j \mathbf{C}_{ij}\right) = \sum_{i=0}^{N} \sum_{j=0}^{N} \left(w_i w_j \rho_{ij} \sigma_i \sigma_j\right) \tag{A3}$$

Because the off diagonal terms of **C** are not known, we evaluate them by estimating the error correlations $\rho_{ij}$ as a Gaussian function of distance $d_{ij}$:

$$\rho_{ij} = e^{-\left(d_{ij}^2 / 2L^2\right)} \tag{A4}$$

Here $L$ is a correlation length that has to be estimated. We then adjust $L$ such that it satisfies the following condition on the reduced $\chi^2$ function with $v = (N-1)^2$ degrees of freedom:

$$\chi_v^2 = \frac{1}{(N-1)^2} \sum_{i=0}^{N} \sum_{j=0}^{N} \frac{\left(y_i - \overline{y}_o\right)\left(y_j - \overline{y}_o\right)}{\rho_{ij} \sigma_i \sigma_j} \rightarrow 1 \tag{A5}$$

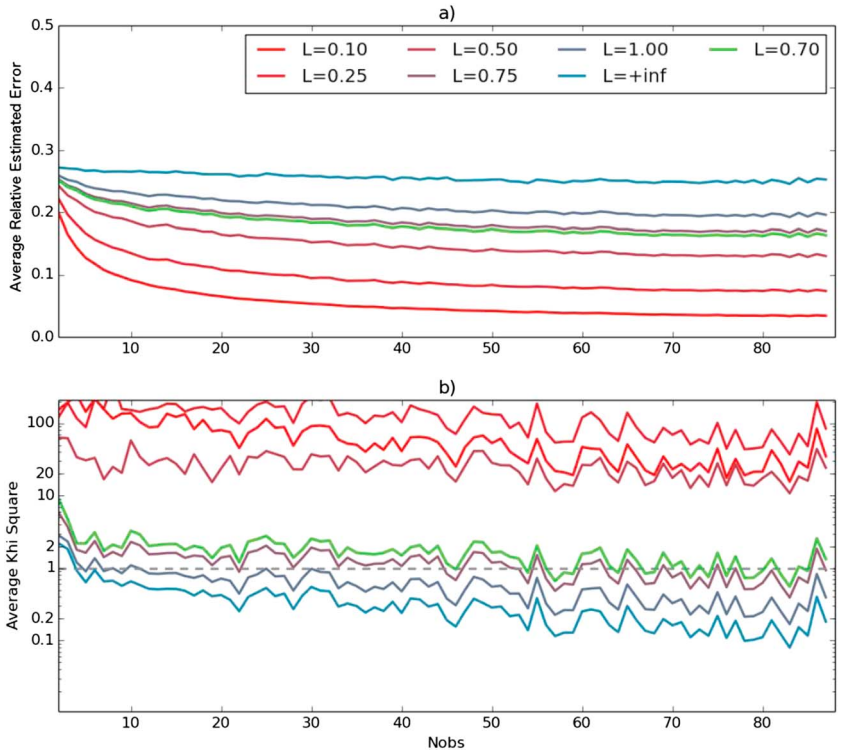


**Figure A1.** (a) Evolution of the average estimated error versus number of observations in a given bin, with varying correlation length. (b) Same as Figure A1a but for $\chi^2_\nu$. Tests are performed for a full day of MOPITT data (1 June 2008) for the 700 hPa vertical level.

Figure A1 shows the $\chi^2_\nu$ versus the number of observations in a given bin for correlation length $L$ ranging from 0.1° to 1°. We found that on average a correlation length of $L = 0.7°$ give the best average $\chi^2_\nu$ match to 1 at global scale and for all IASI and MOPITT levels.

**Acknowledgments**

We would like to acknowledge high-performance computing support from Yellowstone (ark:/85065/d7wd3xhc) provided by NCAR's Computational and Information Systems Laboratory, sponsored by the National Science Foundation. This work was partly supported by NASA grants NNX09AH03G S02, NNX11AI10G, and NNX11AG63G. The National Science Foundation sponsors the National Center for Atmospheric Research. The National Science Foundation and the Office of Science (BER) of the U.S. Department of Energy support the CESM project. The Research in Belgium was funded by the ESA/Belspo IASI. IASI is a joint mission of EUMETSAT and the Centre National d'Etudes Spatiales (CNES, France). Clerbaux is grateful to NCAR and its visitor program, which allowed a fruitful scientific collaboration between the O3MSAF activities. Coheur is Senior Research Associate with F.R.S.-FNRS. IASI and MOPITT teams to develop and to be maintained for years. The surface monitoring data used in this study are available for download from the U.S. EPA's Air Quality System database (http://www.epa.gov/ttn/airs/airsaqs/detaildata/downloadaqsdata.htm). The ARCTAS data used in this study are available for download at http://www-air.larc.nasa.gov/cgi-bin/ArcView/arctas?P3B-MERGE=1. The TES data used in this study are available at http://tes.jpl.nasa.gov/data/. The IASI data used in this study are available at http://www.pole-ether.fr/etherTypo/index.php?id=1585&L=1. The MOPITT data used in this study are available at https://www2.acd.ucar.edu/mopitt. The NCEP data set can be downloaded at http://rda.ucar.edu/datasets/ds337.0/. The CESM code used in this study is available at http://www2.cesm.ucar.edu/models/current.

## References

Anderson, J. L. (2001), An ensemble adjustment Kalman filter for data assimilation, *Mon. Weather Rev.*, *129*, 2884–2903, doi:10.1175/1520-0493(2001)129<2884:AEAKFF>2.0.CO;2.

Anderson, J. L. (2003), A local least squares framework for ensemble filtering, *Mon. Weather Rev.*, *131*, 634–642, doi:10.1175/1520-0493(2003)131<0634:ALLSFF>2.0.CO;2.

Anderson, J. L. (2009), Spatially and temporally varying adaptive covariance inflation for ensemble filters, *Tellus*, *61*, 72–83, doi:10.1111/j.1600-0870.2008.00361.x.

Anderson, J. L., T. Hoar, K. Raeder, H. Liu, N. Collins, R. Torn, and A. Arellano (2009), The data assimilation testbed: A community facility, *Bull. Am. Meteorol. Soc.*, *90*, 1283–1296, doi:10.1175/2009BAMS2618.1.

Arellano, A. F., Jr., K. Raeder, J. L. Anderson, P. G. Hess, L. K. Emmons, D. P. Edwards, G. G. Pfister, T. L. Campos, and G. W. Sachse (2007), Evaluating model performance of an ensemble based chemical data assimilation system during INTEX-B field mission, *Atmos. Chem. Phys.*, *7*, 5695–5710, doi:10.5194/acp-7-5695-2007.

Barré, J., et al. (2014), Combined data assimilation of ozone tropospheric columns and stratospheric profiles in a high-resolution CTM, *Q. J. R. Meteorol. Soc.*, *140*, 966–981, doi:10.1002/qj.2176.

Barré, J., D. Edwards, H. Worden, A. Da Silva, and W. Lahoz (2015), On the feasibility of monitoring carbon monoxide in the lower troposphere from a constellation of Northern Hemisphere geostationary satellites. (Part 1), *Atmos. Environ.*, *113*, 63–77, doi:10.1016/j.atmosenv.2015.04.069.

Beer, R. (2006), TES on the Aura mission: Scientific objectives, measurements, and analysis overview, *IEEE Trans. Geosci. Remote Sens.*, *44*, 1102–1105, doi:10.1109/TGRS.2005.863716.

Beer, R., T. A. Glavich, and D. M. Rider (2001), Tropospheric emission spectrometer for the Earth observing system aura satellite, *Appl. Opt.*, *40*, 2356–2367, doi:10.1364/AO.40.002356.

Bowman, K. W., et al. (2006), Tropospheric emission spectrometer: Retrieval method and error analysis, *IEEE Trans. Geosci. Remote Sens.*, *44*, 1297–1306.

Boynard, A., et al. (2014), First simultaneous space measurements of atmospheric pollutants in the boundary layer from IASI: A case study in the North China Plain, *Geophys. Res. Lett.*, *41*, 645–651, doi:10.1002/2013GL0583332014.

Buehner, M. (2005), Ensemble-derived stationary and flow-dependent background-error covariances: Evaluation in a quasi-operational NWP setting, *Q. J. R. Meteorol. Soc.*, *131*, 1013–1043, doi:10.1256/qj.04.15.

Candille, G., C. Côte, P. L. Houtekamer, and G. Pellerin (2007), Verification of an ensemble prediction system against observations, *Mon. Weather Rev.*, *135*, 2688–2699, doi:10.1175/MWR3414.1.

Claeyman, M., et al. (2010), A linear CO chemistry parameterization in a chemistry-transport model: Evaluation and application to data assimilation, *Atmos. Chem. Phys.*, *10*(13), 6097–6115.

Clerbaux, C., et al. (2008), CO measurements from the ACE-FTS satellite instrument: Data analysis and validation using ground-based, airborne and spaceborne observations, *Atmos. Chem. Phys.*, *8*, 2569–2594, doi:10.5194/acp-8-2569-2008.

Clerbaux, C., et al. (2009), Monitoring of atmospheric composition using the thermal infrared IASI/MetOp sounder, *Atmos. Chem. Phys.*, *9*, 6041–6054, doi:10.5194/acp-9-6041-2009.

Conley, A. J., et al. (2012), Description of the NCAR Community Atmosphere Model (CAM 5.0), NCAR technical note.

De Wachter, E., et al. (2012), Retrieval of MetOp-A/IASI CO profiles and validation with MOZAIC data, *Atmos. Meas. Tech.*, *5*, 2843–2857, doi:10.5194/amt-5-2843-2012.

Deeter, M. N., et al. (2010), The MOPITT version 4 CO product: Algorithm enhancements, validation, and long-term stability, *J. Geophys. Res.*, *115*, D07306, doi:10.1029/2009JD013005.

Deeter, M. N., H. M. Worden, D. P. Edwards, J. C. Gille, D. Mao, and J. R. Drummond (2011), MOPITT multispectral CO retrievals: Origins and effects of geophysical radiance errors, *J. Geophys. Res.*, *116*, D15303, doi:10.1029/2011JD015703.

Deeter, M. N., H. M. Worden, D. P. Edwards, J. C. Gille, and A. E. Andrews (2012), Evaluation of MOPITT retrievals of lower-tropospheric carbon monoxide over the United States, *J. Geophys. Res.*, *117*, D13306, doi:10.1029/2012JD017553.

Deeter, M. N., S. Martínez-Alonso, D. P. Edwards, L. K. Emmons, J. C. Gille, H. M. Worden, J. V. Pittman, B. C. Daube, and S. C. Wofsy (2013), Validation of MOPITT Version 5 thermal-infrared, near-infrared, and multispectral carbon monoxide profile retrievals for 2000–2011, *J. Geophys. Res. Atmos.*, *118*, 6710–6725, doi:10.1002/jgrd.50272.

Deeter, M. N., S. Martínez-Alonso, D. P. Edwards, L. K. Emmons, J. C. Gille, H. M. Worden, C. Sweeney, J. V. Pittman, B. C. Daube, and S. C. Wofsy (2014), The MOPITT Version 6 product: algorithm enhancements and validation, *Atmos. Meas. Tech.*, *7*(11), 3623–3632, doi:10.5194/amt-7-3623-2014.

Desroziers, G., L. Berre, B. Chapnik, and P. Poli (2005), Diagnosis of observation, background and analysis-error statistics in observation space, *Q. J. R. Meteorol. Soc.*, *131*, 3385–3396, doi:10.1256/qj.05.108.

Drummond, J. R., J. Zou, F. Nichitiu, J. Kar, R. Deschambaut, and J. Hackett (2010), A review of 9-year performance and operation of the MOPITT instrument, *J. Adv. Space Res.*, doi:10.1016/j.asr.2009.11.019.

El Amraoui, L., et al. (2010), Midlatitude stratosphere-troposphere exchange as diagnosed by MLS O3 and MOPITT CO assimilated fields, *Atmos. Chem. Phys.*, *10*, 2175–2194, doi:10.5194/acp-10-2175-2010.

El Amraoui, L., J.-L. Attié, P. Ricaud, W. A. Lahoz, A. Piacentini, V.-H. Peuch, J. X. Warner, R. Abida, J. Barré, and R. Zbinden (2014), Tropospheric CO vertical profiles deduced from total columns using data assimilation: Methodology and validation, *Atmos. Meas. Tech.*, *7*, 3035–3057, doi:10.5194/amt-7-3035-2014.

Emmons, L. K., et al. (2010), Description and evaluation of the Model for Ozone and Related chemical Tracers, version 4 (MOZART-4), *Geosci. Model Dev.*, *3*, 43–67, doi:10.5194/gmd-3-43-2010.

Emmons, L. K., et al. (2015), The POLARCAT Model Intercomparison Project (POLMIP): Overview and evaluation with observations, *Atmos. Chem. Phys.*, *15*, 6721–6744, doi:10.5194/acp-15-6721-2015.

Evensen, G. (1994), Sequential data assimilation with a nonlinear quasigeostrophic model using Monte-Carlo methods to forecast error statistics, *J. Geophys. Res.*, *99*, 10,143–10,162, doi:10.1029/94JC00572.

Evensen, G. (2003), The ensemble Kalman filter: Theoretical formulation and practical implementation, *Ocean Dyn.*, *53*, 343–367, doi:10.1007/s10236-003-0036-9.

Fortems-Cheiney, A., F. Chevallier, I. Pison, P. Bousquet, C. Carouge, C. Clerbaux, P.-F. Coheur, M. George, D. Hurtmans, and S. Szopa (2009), On the capability of IASI measurements to inform about CO surface emissions, *Atmos. Chem. Phys.*, *9*, 8735–8743, doi:10.5194/acp-9-8735-2009.

Gaspari, G., and S. E. Cohn (1999), Construction of correlation functions in two and three dimensions, *Q. J. R. Meteorol. Soc.*, *125*, 723–757, doi:10.1002/qj.49712555417.

Gaubert, B., A. Coman, G. Foret, F. Meleux, A. Ung, L. Rouil, A. Ionescu, Y. Candau, and M. Beekmann (2014), Regional scale ozone data assimilation using an ensemble Kalman filter and the CHIMERE chemical transport model, *Geosci. Model Dev.*, *7*, 283–302, doi:10.5194/gmd-7-283-2014.

George, M., et al. (2015), An examination of the long-term CO records from MOPITT and IASI: Comparison of retrieval methodology, *Atmos. Meas. Tech. Discuss.*, *8*, 4095–4135, doi:10.5194/amtd-8-4095-2015.

Griffin, R. J., J. Chen, K. Carmody, and S. Vutukuru (2007), Contribution of gas phase oxidation of volatile organic compounds to atmospheric carbon monoxide levels in two areas of the united States, *J. Geophys. Res.*, *11*, D10S17, doi:10.1029/2006JD007602.

Guenther, A. B., X. Jiang, C. L. Heald, T. Sakulyanontvittaya, T. Duhl, L. K. Emmons, and X. Wang (2012), The model of emissions of gases and aerosols from nature version 2.1 (MEGAN2.1): An extended and updated framework for modeling biogenic emissions, *Geosci. Model Dev.*, *5*, 1471–1492, doi:10.5194/gmd-5-1471-2012.

Hurtmans, D., P.-F. Coheur, C. Wespes, L. Clarisse, O. Scharf, C. Clerbaux, J. Hadji-Lazaro, M. George, and S. Turquety (2012), FORLI radiative transfer and retrieval code for IASI, *J. Quant. Spectros. Radiat. Transfer*, *113*, 1391–1408, doi:10.1016/j.jqsrt.2012.02.036.

Inness, A., et al. (2013), The MACC reanalysis: An 8 yr data set of atmospheric composition, *Atmos. Chem. Phys.*, *13*(8), 4073–4109, doi:10.5194/acp-13-4073-2013.

Jiang, Z., D. B. A. Jones, H. M. Worden, M. N. Deeter, D. K. Henze, J. Worden, K. W. Bowman, C. A. M. Brenninkmeijer, and T. J. Schuck (2013), Impact of model errors in convective transport on CO source estimates inferred from MOPITT CO retrievals, *J. Geophys. Res. Atmos.*, *118*, 2073–2083, doi:10.1002/jgrd.50216.

Kanakidou, M., and P. J. Crutzen (1999), The photochemical source of carbon monoxide: Importance, uncertainties, and feedbacks, *Chemosphere Global Change Sci.*, *1*, 91–109, doi:10.1016/S1465-9972(99)00022-7.

Kerzenmacher, T., et al. (2012), Validation of IASI FORLI carbon monoxide retrievals using FTIR data from NDACC, *Atmos. Meas. Tech.*, *5*, 2751–2761, doi:10.5194/amt-5-2751-2012.

Klonecki, A., et al. (2012), Assimilation of IASI satellite CO fields into a global chemistry transport model for validation against aircraft measurements, *Atmos. Chem. Phys.*, *12*, 4493–4512, doi:10.5194/acp-12-4493-2012.

Lamarque, J.-F., et al. (2004), Application of a bias estimator for the improved assimilation of Measurements of Pollution in the Troposphere (MOPITT) carbon monoxide retrievals, *J. Geophys. Res.*, *109*, D16304, doi:10.1029/2003JD004466.

Lamarque, J.-F., et al. (2010), Historical (1850–2000) gridded anthropogenic and biomass burning emissions of reactive gases and aerosols: Methodology and application, *Atmos. Chem. Phys.*, *10*, 7017–7039, doi:10.5194/acp-10-7017-2010.

Lamarque, J.-F., et al. (2012), CAM-chem: Description and evaluation of interactive atmospheric chemistry in the community Earth system model, *Geosci. Model Dev.*, *5*, 369–411, doi:10.5194/gmd-5-369-2012.

Luo, M., et al. (2007a), Carbon monoxide measurements by TES and MOPITT – The influence of a priori data and instrument characteristics on nadir atmospheric species retrievals, *J. Geophys. Res.*, *112*, D09303, doi:10.1029/2006JD007663.

Luo, M., et al. (2007b), TES carbon monoxide validation with DACOM aircraft measurements during INTEX-B 2006, *J. Geophys. Res.*, *112*, D24S48, doi:10.1029/2007JD008803.

Miyazaki, K., H. J. Eskes, K. Sudo, M. Takigawa, M. van Weele, and K. F. Boersma (2012), Simultaneous assimilation of satellite $NO_2$, $O_3$, CO, and $HNO_3$ data for the analysis of tropospheric chemical composition and emissions, *Atmos. Chem. Phys.*, *12*, 9545–9579, doi:10.5194/acp-12-9545-2012.

Monks, S. A., et al. (2015), Multi-model study of chemical and physical controls on transport of anthropogenic and biomass burning pollution to the Arctic, *Atmos. Chem. Phys.*, *15*, 3575–3603, doi:10.5194/acp-15-3575-2015.

Myhre, G., D. Shindell, F. Bréon, W. Collins, J. Fuglestvedt, J. Huang, D. Koch, J. Lamarque, D. Lee, and B. Mendoza (2013), Anthropogenic and natural radiative forcing, in *Climate change 2013: The Physical Science Basis. Contribution of Working Group I to the Fifth Assessment Report of the Intergovernmental Panel on Climate Change*, edited by T. F. Stocker et al., pp. 658–740, Cambridge Univ. Press, Cambridge, U.K., and New York.

Parrish, D. F., and J. C. Derber (1992), The national meteorological center's spectral statistical-interpolation analysis system, *Mon. Weather Rev.*, *120*, 1747–1763, doi:10.1175/1520-0493(1992)120<1747:TNMCSS>2.0.CO;2.

Pfister, G. G., J. Avise, C. Wiedinmyer, D. P. Edwards, L. K. Emmons, G. D. Diskin, J. Podolske, and A. Wisthaler (2011), CO source contribution analysis for California during ARCTAS-CARB, *Atmos. Chem. Phys.*, *11*, 7515–7532, doi:10.5194/acp-11-7515-2011.

Raeder, K., J. L. Anderson, N. Collins, T. J. Hoar, J. E. Kay, P. H. Lauritzen, and R. Pincus (2012), DART/CAM: An ensemble data assimilation system for CESM atmospheric models, *J. Clim.*, *25*, 6304–6317, doi:10.1175/JCLI-D-11-00395.1.

Rinsland, C. P., et al. (2006), Nadir measurements of carbon monoxide distributions by the Tropospheric Emission Spectrometer instrument onboard the Aura spacecraft: Overview of analysis approach and examples of initial results, *Geophys. Res. Lett.*, *33*, L22806, doi:10.1029/2006GL027000.

Rodgers, C. D. (2000), *Inverse Methods for Atmospheric Sounding – Theory and Practise*, *Series on Atmos., Oceanic Planet. Phys.*, vol. 2, World Scientific, Singapore.

Shindell, D. T., et al. (2006), Multimodel simulations of carbon monoxide: Comparison with observations and projected near-future changes, *J. Geophys. Res.*, *111*, D19306, doi:10.1029/2006JD007100.

Stein, O., M. G. Schultz, I. Bouarar, H. Clark, V. Huijnen, A. Gaudel, M. George, and C. Clerbaux (2014), On the wintertime low bias of Northern Hemisphere carbon monoxide found in global model simulations, *Atmos. Chem. Phys.*, *14*, 9295–9316, doi:10.5194/acp-14-9295-2014.

Tilmes, S., et al. (2015), Description and evaluation of tropospheric chemistry and aerosols in the Community Earth System Model (CESM1.2), *Geosci. Model Dev.*, *8*, 1395–1426, doi:10.5194/gmd-8-1395-2015.

Turquety, S., D. Hurtmans, J. Hadji-Lazaro, P.-F. Coheur, C. Clerbaux, D. Josset, and C. Tsamalis (2009), Tracking the emission and transport of pollution from wildfires using the IASI CO retrievals: analysis of the summer 2007 Greek fires, *Atmos. Chem. Phys.*, *9*, 4897–4913, doi:10.5194/acp-9-4897-2009.

von Clarmann, T., and U. Grabowski (2007), Elimination of hidden a priori information from remotely sensed profile data, *Atmos. Chem. Phys.*, *7*, 397–408, doi:10.5194/acp-7-397-2007.

Wiedinmyer, C., S. K. Akagi, R. J. Yokelson, L. K. Emmons, J. A. Al-Saadi, J. J. Orlando, and A. J. Soja (2011), The Fire INventory from NCAR (FINN): A high resolution global model to estimate the emissions from open burning, *Geosci. Model Dev.*, *4*, 625–641, doi:10.5194/gmd-4-625-2011.

Worden, H. M., M. N. Deeter, D. P. Edwards, J. C. Gille, J. R. Drummond, and P. Nedelec (2010), Observations of near-surface carbon monoxide from space using MOPITT multispectral retrievals, *J. Geophys. Res.*, *115*, D18314, doi:10.1029/2010JD014242.

Worden, H. M., et al. (2013), Decadal record of satellite carbon monoxide observations, *Atmos. Chem. Phys.*, doi:10.5194/acp-13-837-2013.

Yudin, V. A., G. Pétron, J.-F. Lamarque, B. V. Khattatov, P. G. Hess, L. V. Lyjak, J. C. Gille, D. P. Edwards, M. N. Deeter, and L. K. Emmons (2004), Assimilation of the 2000–2001 CO MOPITT retrievals with optimized surface emissions, *Geophys. Res. Lett.*, *31*, L20105, doi:10.1029/2004GL021037.

Zhang, L., D. J. Jacob, X. Liu, J. A. Logan, K. Chance, A. Eldering, and B. R. Bojkov (2010), Intercomparison methods for satellite measurements of atmospheric composition: Application to tropospheric ozone from TES and OMI, *Atmos. Chem. Phys.*, *10*, 4725–4739, doi:10.5194/acp-10-4725-2010.